

Department of Physics and Astronomy  
University of Heidelberg

Master Thesis in Physics

submitted by

**Michael Straub**

born in Penarth (United Kingdom)

**2021**

# Multiphoton Ionization of Helium with Extreme Ultraviolet Light at the Free-Electron Laser in Hamburg

This Master Thesis has been carried out by Michael Straub at the  
Max Plank Institut für Kernphysik in Heidelberg  
under the supervision of  
Prof. Dr. Thomas Pfeifer  
and co-supervisor  
Dr. Christian Ott

## **Abstract**

In this thesis, multi-photon ionization of helium is studied using extreme ultraviolet (XUV) light from the Free Electron Laser in Hamburg (FLASH). The highly correlated electron dynamics is measured indirectly by recoil-ion momentum spectroscopy using a reaction microscope. In addition, a new XUV photon spectrometer is used to measure the incoming FEL spectra on a shot-to-shot basis at 100 kHz repetition rate. With a resolution well below 100 meV, the intrinsic pulse structure of the FEL can be resolved. Numerical results validate a novel technique that combines recoil-ion and photon spectroscopy to measure two-photon resonances at resolutions below the FEL-bandwidth. First experimental results probing a two-photon Fano-resonance in helium at 30 eV photon energy are presented.

In addition, two-photon double ionization is measured in the sequential and direct regime at photon energies between 40 eV and 57 eV. We are able to observe the emergence of the virtual sequential process and compare the results with calculations solving the Schrödinger equation.

## **Zusammenfassung**

In dieser Arbeit wird die Multiphotonen-Ionisation von Helium mit extrem ultravioletten Pulsen am Freien Elektronenlaser (FEL) in Hamburg (FLASH) untersucht. Die hochkorrelierte Elektronendynamik wird indirekt durch Rückstoß-Ionenimpulsspektroskopie mit einem Reaktionsmikroskop gemessen. Zusätzlich wird ein neues XUV-Photonen-Spektrometer eingesetzt, um die eintreffenden FEL-Spektren Schuss für Schuss bei einer Wiederholrate von 100 kHz im Burst-Modus zu messen. Mit einer Auflösung von weit unter 100 meV wird die intrinsische Pulsstruktur des FEL erkennbar. Numerische Simulationen zeigen eine neue Technik, die die Rückstoß-Ionen- und Photonenspektroskopie kombiniert, um Zwei-Photonen-Resonanzen mit einer Auflösung unterhalb der Laserbandbreite zu messen.

Experimentell wird die Zwei-Photonen-Ionisierung oberhalb der Ionisationsschwelle bei einer Photonenenergie von etwa 30 eV untersucht. Diese liegt in der Nähe von doppelt angeregten Fano-Resonanzen in Helium. Des Weiteren wurde die Zwei-Photonen-Doppelionisation im sequentiellen und direkten Bereich zwischen 40 eV und 57 eV untersucht. Wir können das Aufkommen des virtuellen sequentiellen Prozesses nachweisen und mit Ergebnissen aus Berechnungen mit der Schrödinger-Gleichung vergleichen.

# Contents

<b>1</b>	<b>Introduction</b>	<b>1</b>
<b>2</b>	<b>Fundamental theory</b>	<b>4</b>
2.1	Non-relativistic light-matter interaction . . . . .	4
2.2	Few-level system . . . . .	5
2.3	Photoionization . . . . .	6
2.3.1	Momentum distribution . . . . .	7
2.3.2	Autoionization . . . . .	8
2.3.3	Multi-ionization processes . . . . .	10
2.4	Helium atom . . . . .	11
<b>3</b>	<b>Experimental Setup</b>	<b>14</b>
3.1	Free electron laser physics at FLASH . . . . .	14
3.2	Reaction Microscope . . . . .	18
3.3	Absorption spectroscopy beamline . . . . .	21
3.4	Commissioning measurements . . . . .	23
3.4.1	Energy calibration . . . . .	24
3.4.2	Determination of spectral resolution . . . . .	24
3.4.3	REMI-Spectrometer correlation . . . . .	26
<b>4</b>	<b>Above Threshold Ionization in Helium</b>	<b>28</b>
4.1	Numerical calculations . . . . .	28
4.1.1	Rate equations . . . . .	29
4.1.2	Few-level simulation . . . . .	31
4.2	Experiment . . . . .	35
4.2.1	Linear process . . . . .	37
4.2.2	Space-charge effect . . . . .	38
4.2.3	Two-photon process . . . . .	38
4.3	Discussion and Outlook . . . . .	41

<b>5</b>	<b>Multi-Photon Double Ionization in Helium</b>	<b>43</b>
5.1	Ab initio theory . . . . .	44
5.2	Experiment . . . . .	45
5.2.1	Sequential Ionization at 57 eV . . . . .	45
5.2.2	Direct Double Ionization at 45 eV . . . . .	47
5.2.3	Virtual sequential Ionization at 53 eV . . . . .	49
5.2.4	Resonant three-photon sequential double ionization at 40.8 eV	51
5.3	Discussion and Outlook . . . . .	53
<b>6</b>	<b>Conclusions</b>	<b>56</b>
<b>7</b>	<b>Appendix</b>	<b>58</b>
7.1	Momentum reconstruction in a Reaction Microscope . . . . .	58
7.2	Parameter of few-level system . . . . .	59
7.3	Split step method . . . . .	60

# 1 Introduction

With the advent of free electron lasers (FELs), a new light source with high brilliance has become available to probe the dynamics of atoms and molecules. The free electron laser in Hamburg (FLASH) operates from the extreme ultraviolet (XUV) to the soft x-ray wavelength regime [1] and therefore allows to excite atoms at their intrinsic energy scale. In addition, the pulses are only a couple of femtoseconds (fs) long and allow for a temporal well-defined initiation of photoionization or photoexcitation. The high intensity of the FEL pulses, on the other hand, opens nonlinear channels of the interaction process. The employed Reaction Microscopes (REMI) allows for three-dimensional momentum reconstruction of all charged fragments after ionization[2]. The combination of REMI and FEL allows for previously unattainable measurements of detection and understanding of different ionization and dissociation channels.

The presented experiments have been conducted at the FLASH2 FL26 REMI beamline where the FEL wavelength can be quickly adjusted. The photon source operates in the so-called self amplified spontaneous emission (SASE) mode. SASE has an intrinsic stochastic pulse structure due to the the stochastic nature of the spontaneous emission. A single pulse is made up of multiple sub-pulses in time and several spikes in the energy spectrum. The bandwidth of the FEL is usually an order of magnitude wider than the width of the individual spikes in the energy spectrum. To access the spectral structure of FEL pulses, a photon spectrometer can be used.

The combination of using a REMI to distinguish different ionization and dissociation channels together with the photon energy resolution given by a photon spectrometer provides new unique possibilities. For instance, it can provide new insights into the bound or quasi-bound electron configurations, which are crucial in understanding the fundamental electromagnetic interaction. The smallest bound multi-electron system is helium with two electrons bound to a core. Helium provides a rich assortment of interesting physical phenomena including double electron excitations[3, 4] and highly correlated double ionization processes[5].

## 1. Introduction

---

There is no analytic solution to the quantum three-body problem and numerical approaches provide a serious challenge. Compared to atoms with an increased number of electrons, fewer approximations are needed for feasible theoretical calculations[6]. Therefore, in this thesis, helium will be the benchmark system of choice.

In the first presented experiment, doubly excited autoionizing states of helium are driven by a two-photon transition from the atomic ground state. Contrary to states excited with a single photon, excitations with two photons have an even system symmetry. Therefore, the two-photon process probes a whole different class of resonances compared to the linear process. Compared to the bandwidth of the FEL, the two-photon resonances are expected to be narrower[4]. In this work, an approach to resolve a two-photon resonance with stochastic spiky FEL spectra is presented and numerically evaluated. In addition, first experimental results probing the  $2p2p\ ^1D^e$  doubly excited state are presented<sup>1</sup>.

In contrast to the first experiment which focuses on quasi-bound electron interaction, the second experiment probes the interaction of two electrons in their continuum states. If the photon energy exceeds the second ionization threshold of 54.4 eV, after the first electron is ionized, the second electron can be ionized individually. In contrast to this, in the energy range between 39.5 eV and 54.4 eV, the electrons have to share energy to be doubly ionized. Energy is shared due to the high correlation of both electrons in their bound state. If emitted simultaneously, the electrons remain highly correlated. Two-photon double ionization provides a rich benchmark, probing the induced correlation of the infinite-range Coulomb interaction. The second experiment is carried out at FEL-photon energies of 40.8 eV, 45 eV, 53 eV and 57 eV where different ionization channels come to the fore. Uncorrelated electrons are observed at a photon energy of 57 eV in contrast to highly correlated electrons at 45 eV. Increasing the photon energy close to the second ionization threshold introduces a channel called virtual sequential ionization[9]. Finally, Rydberg resonances of the  $\text{He}^+$  ion (e.g. at 40.8 eV) enhance the possibility for a sequential three-photon double ionization.

---

<sup>1</sup>the correct classification using hyperspherical quantum numbers[7, 8] is neglected in favor of an easier comprehensible illustration



## 1. Introduction

---

This thesis is organized as follows: In chapter §2, the fundamental physical background needed to understand the experiments is introduced. The experimental setup is shown in chapter§3, as well as initial commissioning results. The next chapter §4 is focused on the two-photon excited states and shows numerical, as well as first experimental results. Chapter §5 introduces theoretical background for ab-initio calculations concerning double ionization before showing the main experimental results. Finally, in the last chapter §6, a summary and conclusion is drawn.

Throughout the thesis, multiple quantities will be given in Hartree atomic units[10]. This natural unit system is defined by four fundamental physical constants set to unity: the reduced Planck constant  $\hbar$ , the elementary charge  $e$ , the Bohr radius  $a_0$  and the electron mass  $m_e$ . Atomic units will be abbreviated either by a.u. or au.

## 2 Fundamental theory

For the experiments described within this thesis, XUV radiation was used with intensities of up to  $\sim 1 \times 10^{14} \text{ W cm}^{-2}$ . Ab initio calculations for three partite systems like Helium are quite complicated, especially in a non-perturbative quantum regime[4, 11–13].

The following chapter covers only a fundamental understanding of the theory that is needed to understand the experiments in this work. Starting with basic light matter interaction, we will discuss the dipole approximation and few-level systems. In §2.3 several different ionization processes will be discussed. The last section describes experimentally important features of Helium.

### 2.1 Non-relativistic light-matter interaction

In a classical picture, the properties of light and its propagation through space can be fully described using Maxwell's equations. One solution to the Maxwell equation is the propagating electromagnetic wave with an vector potential  $\mathbf{A}(\mathbf{r}, t)$ , wave vector  $\mathbf{k}$  and frequency  $\omega$ ,

$$\mathbf{A}(\mathbf{r}, t) = \mathbf{A}_0 \cdot \left( e^{i(\mathbf{k}\mathbf{r} - \omega t)} + e^{-i(\mathbf{k}\mathbf{r} - \omega t)} \right). \quad (2.1)$$

The amplitude  $\mathbf{A}_0$  can be complex to describe the polarization.

The quantum mechanical description of a particle is performed via the Schrödinger equation

$$i\hbar \frac{\partial}{\partial t} \Psi = \mathcal{H} \Psi = \left( \frac{p^2}{2m} + V \right) \Psi. \quad (2.2)$$

To include the effect of the classical potential  $\mathbf{A}$ , we can make a transformation

$$\mathbf{p} \rightarrow \mathbf{p} - e\mathbf{A} \quad (2.3)$$

$$\mathcal{H} = \frac{1}{2m} (\mathbf{p} - e\mathbf{A})^2 + V \quad (2.4)$$

which reproduces the classical equations of motion.

For all electromagnetic radiation employed in this work, the wavelength  $\lambda$  is much larger than the target atom. Therefore the so-called dipole approximation  $\mathbf{A}(r, t) \simeq \mathbf{A}(r_0, t)$  is valid.

Performing a unitary transformation we construct a Hamiltonian linear in the electric field  $\mathbf{E} = -\frac{\partial \mathbf{A}}{\partial t}$ .

$$\mathcal{H} = \underbrace{\frac{p^2}{2m}}_{\mathcal{H}_0} + V \underbrace{-\hat{d}\mathbf{E}}_{\mathcal{H}_I}, \quad (2.5)$$

with the dipole operator  $\hat{d} = e \mathbf{r}$ .

## 2.2 Few-level system

The earliest accomplishment of quantum mechanics was to derive the energy levels of hydrogen[14]. The generic structure of atoms consists of a ground state  $|g\rangle$ , multiple excited states  $|e_i\rangle$  and a continuum of momentum states  $|k\rangle$  if the energy of the system is above its ionization threshold.

Instead of relying on ab-initio methods to calculate the details of an atom, we can use its energy levels to simplify its description. In many cases it is sufficient to select a subset of states to describe the key physical features of a system. The system is then finite and the Hamiltonian can be written in matrix notation  $\mathcal{H}_{ij} = \langle i | \mathcal{H} | j \rangle$ . The diagonal elements  $\mathcal{H}_{ii}$  are the energy of individual states, while off-diagonal elements represent the interaction between states. Most interaction is driven by the electromagnetic field and can be calculated via the dipole operator  $\mathcal{H}_{fi} = \langle f | -\hat{d}E(t) | i \rangle$ .

Atoms will have energy levels associated to quantum numbers. Of high interest is the angular momentum quantum number  $l$ . The dipole operator is only non-zero if  $l$  differs by exactly one between the initial and final state. All other transitions are dipole forbidden. In the photon picture, this means that each absorbed photon either adds or subtracts angular momentum.

A two-level system is already sufficient to describe multiple important phenomena, for instance the population transfer, known as Rabi-oscillation[15], as well as the electromagnetic field shift of the energy levels of the system, also

known as AC Stark shift[16].

$$\mathcal{H} = \begin{pmatrix} E_i & d_{ij} \cdot E(t) \\ d_{ij}^* \cdot E(t) & E_j \end{pmatrix} \quad (2.6)$$

In most realistic situations one also has to consider a coupling to the environment, which leads to the decay of excited states. Instead of an open system approach[17], we can include the decay by introducing complex energies with a decay width  $\Gamma$ [18]:

$$\mathcal{E} = E - i\frac{\Gamma}{2} \quad (2.7)$$

In this work, continuum states will be described by single virtual states with large values of  $\Gamma$ , which represent the flat cross-section reasonable in the region of interest. The lifetime of such a virtual state is approximately given by the Heisenberg's uncertainty relation. In this picture a continuum state can be further coupled to other states, either by a free interaction or due to the electromagnetic field.

## 2.3 Photoionization

Photoionization is the interaction between electromagnetic waves and bound electrons that ends up in the removal of one or more electrons. The ionization process gives access to information on the original system itself. Therefore, photoionization is used in many fields of science and technology.

Keldysh introduced a parameter to distinguish if processes can be described by classical fields or have to be described in a quantized manner[19]. Both experiments presented in this work have a Keldysh-parameter much higher than one, which means that we have to treat ionization in the multi-photon picture.

For linear processes, the rate of ions produced through photoionization  $N^+$  is given by the differential equation

$$\frac{dN^+}{dt} = \sigma_1 \Phi N, \quad (2.8)$$

given the photoionization cross-section  $\sigma_1$  and the photon flux  $\Phi$ . The linear process describes single-photon interaction.

---

## 2. Fundamental theory

---

The flux  $\Phi$  is given by the intensity of the incident light pulse  $I$  divided by the photon energy  $\hbar\omega$ . Integrating over the pulse duration, one finds that the total number of produced ions is given by the pulse energy  $\mathcal{E}$ , independent of the pulse structure:

$$N^+(t \rightarrow \infty) = N_0 \left( 1 - \exp \left( -\sigma_1 \int dt \left( \frac{I}{\hbar\omega} \right) \right) \right) = N_0 \left( 1 - e^{-\sigma_1 \frac{\mathcal{E}}{\hbar\omega}} \right) \quad (2.9)$$

The rate equation (2.8) can be generalized to n-th order for multi-photon processes:

$$\frac{dN^+}{dt} = \sigma_n \left( \frac{I}{\hbar\omega} \right)^n N, \quad (2.10)$$

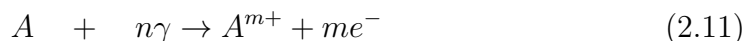
where  $\sigma_n$  is the generalized n-photon cross-section[20]. It has units of  $\text{cm}^{2n}\text{s}^{n-1}$ .

The total number of ions produced is now highly dependent on the pulse structure. Nonlinear contributions are favored by high peak intensities. To favor nonlinear over linear processes, a small pulse energy with high peak intensity is desired. Experimentally this can be accomplished by a short pulse duration and small focus sizes.

In multi-photon ionization, an electron can be emitted when the incoming photons have in total more energy than the ionization potential. The multi-photon process is called above threshold ionization (ATI) when more photons ionize the atom than are energetically necessary to do so[21]. In principle this effect will be highly unlikely, but it can be enhanced by resonances due to autoionizing states (§2.3.2).

### 2.3.1 Momentum distribution

One can gather information of the system by investigating the momentum distribution of the ionized electrons. The reaction channel with  $n$  photons and  $m$  ionized electrons is:



Without loss of generality, we can assume the initial momenta of the atom  $A$  to be zero. Using momentum conservation we can calculate

$$n\mathbf{p}_\gamma = \mathbf{p}_{A^{m+}} + \sum_m \mathbf{p}_m. \quad (2.12)$$

---

## 2. Fundamental theory

---

A quick evaluation shows that the photon momentum  $p_\gamma$  is negligible in most real cases. Energy conservation implies:

$$n\omega = \frac{p_{A^{m+}}^2}{2m_A} + \sum_m \frac{p_m^2}{2m_e} + E_I, \quad (2.13)$$

with  $E_I$  given by the ionization threshold.

In the case of single ionization we can calculate the absolute momentum analytically:

$$\mathbf{p}_e = \sqrt{(n\hbar\omega - E_I) \left( \frac{1}{2m_e} + \frac{1}{2m_A} \right)^{-1}} \quad (2.14)$$

$$\mathbf{p}_A = -\mathbf{p}_e \quad (2.15)$$

After ionization, information on the systems quantum numbers is still imprinted in the momentum distribution of the photoelectron. The orbital angular momentum distribution for specific quantum numbers  $l, m$  can be calculated by the spherical harmonic functions  $Y_{l,m}(\theta, \phi)$ . The experiments described within this thesis use linearly polarized light, which does not change  $m$ . Right or left circularly polarized photon introduce  $\Delta m = \pm 1$ .

We study Helium targets initially in the ground state. The only break from spherical symmetry is introduced by linear polarization of the incident laser light. The polarization acts as the only assigned direction. The angular dependence can therefore be given by the angle  $\theta$  between the polarization and momentum.

The momentum distribution of the first three angular momenta are:

$$l = 0 : \quad |Y_{0,0}(\theta)|^2 = \frac{1}{4\pi} \quad (2.16)$$

$$l = 1 : \quad |Y_{1,0}(\theta)|^2 = \frac{3}{4\pi} \cos^2(\theta) \quad (2.17)$$

$$l = 2 : \quad |Y_{2,0}(\theta)|^2 = \frac{5}{16\pi} (3 \cos^2(\theta) - 1)^2 \quad (2.18)$$

The equations are visualized in Figure 2.1.

### 2.3.2 Autoionization

In multi-electron systems, the Coulomb-interaction between electrons can lead to excitations of multiple correlated electrons. We can find entangled electronic configurations with a total energy above the ionization threshold[22].

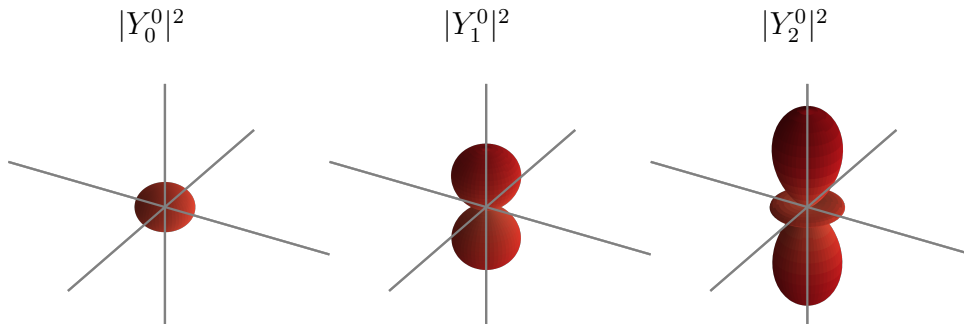


Figure 2.1: The momentum distribution calculated with the spherical harmonics up to  $l = 2$ .

The entangled state with an energy above the ionization threshold will couple with the continuum of momentum states. The state will automatically decay into ionization. The autoionizing state opens a second channel into the continuum which can quantum mechanically interfere with the direct path into the continuum. The ionization cross-section features an asymmetric line shape because of this interference.

A theoretical description was developed by Fano[3]. He used a toy system in dipole approximation given by the ground state  $|g\rangle$ , an excited state with defined energy  $|e\rangle$  and continuum states  $|\chi_E\rangle$  with energies  $E$ . The non-zero dipole moments are given by  $d_e = \langle e|\mathcal{H}|g\rangle$  and  $d_c = \langle \chi_E|\mathcal{H}|g\rangle$ . A free interaction  $V = \langle e|\mathcal{H}|\chi\rangle$  between the excited state and the continuum is also added.

The toy model can be solved by finding the eigenstates  $|\Psi_E\rangle$  given by

$$\mathcal{H}|\Psi_E\rangle = E|\Psi_E\rangle. \quad (2.19)$$

$|\Psi_E\rangle$  is a superposition of continuum state  $|\chi_E\rangle$  and bound state  $|e\rangle$ .

Fano found that the expectation value for an transition  $\hat{T}$  between ground state and continuum is modified due to the resonant state by

$$\frac{|\langle \Psi_E|\hat{T}|g\rangle|^2}{|\langle \chi_E|\hat{T}|g\rangle|^2} = \frac{(q\Gamma/2 + E - E_{res})^2}{(\Gamma/2)^2 + (E - E_{res})^2} \quad (2.20)$$

This expression includes the asymmetry parameter  $q$

$$q = \frac{d_e}{\pi V^* d_c}, \quad (2.21)$$

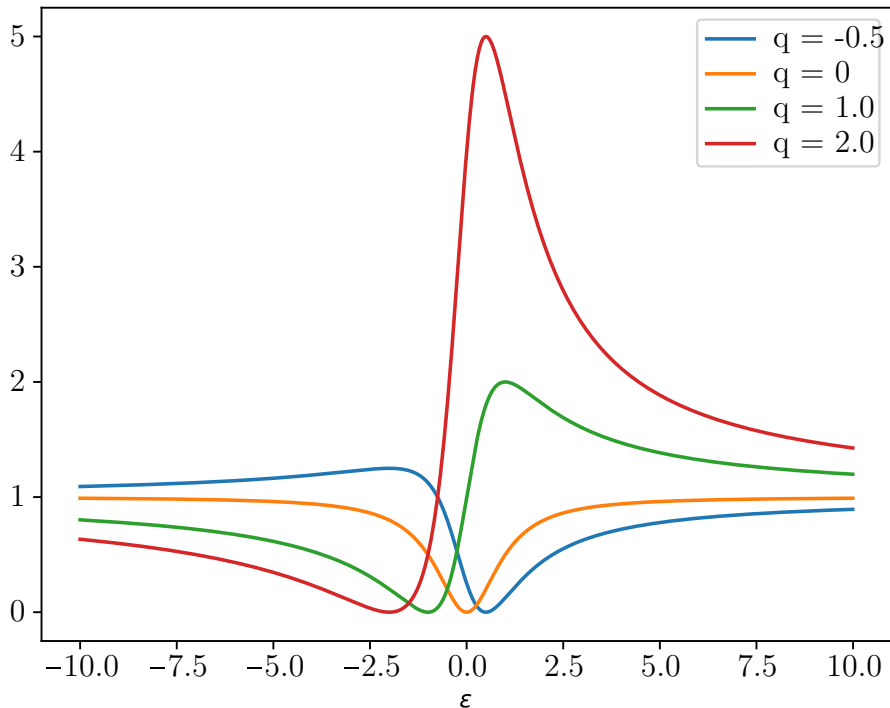


Figure 2.2: Fano resonance curves for different  $q$  parameters.

the resonant energy position  $E_{res}$  and the decay width  $\Gamma$ . For  $q = 0$  we recover the usual Lorentz line-shape. Fitting a cross-section is done with the expression

$$\sigma = a \cdot \frac{|q + \varepsilon|^2}{1 + \varepsilon^2} + \sigma_{NR}. \quad (2.22)$$

The parameter  $a$  scales the effect compared to the non-resonant background  $\sigma_{NR}$ . For simplification the reduced energy  $\varepsilon$  is used:

$$\varepsilon = \frac{E - E_{res}}{\Gamma/2}. \quad (2.23)$$

### 2.3.3 Multi-ionization processes

Between 25.6 eV and 79.0 eV one photon is enough to singly ionize an Helium atom, but not the second electron. Two or three-photon interaction is needed for double ionization. In this thesis, we will distinguish between two multi-photon multi-ionization channels.

The first channel is called sequential ionization. It is a step-by-step process of absorbing photons needed for individual ionization. Between the ionization pro-



cesses, the system relaxes into the respective systems ground state. The electrons are individually excited and have uncorrelated dynamics.

The second channel is direct ionization. Multiple photons interact with the system before the first electron leaves the system quite similar to ATIs. If the total energy of photons is over the second ionization potential, the electrons can share the energy and leave the system. Compared to sequential ionization, the electrons can be highly correlated, as they are emitted together.

Experiments with argon showed that the sequential ionization process dominates[23, 24]. Theory investigating helium shows similar results[25]. The direct process can still be investigated by tuning the photon energy to where the sequential process is energetically forbidden.

For photon energies close to the minimal energy for the sequential process, a virtual sequential process happens. The first electron is lost, but the configuration of the second electron is not necessarily relaxed into the ground state of the helium ion. Therefore, the energy of the second electron directly after ionization is not well defined. Another photon can use the uncertainty in energy and ionize the second electron.

## 2.4 Helium atom

The helium atom is the simplest multi-electronic system and is therefore the perfect benchmark to challenge complicated two-electron interaction. In this work, we will study electron-electron interaction induced by nonlinear light interaction.

The true classification of two-electron states is given by correlated quantum numbers  $_{N}(K, T)_n$ [7, 8]. For simplification this work uses the approximate independent electronic configuration and the fundamental symmetry to describe states:

$$nl_1ml_2 \ ^{2S+1}L^\pi. \quad (2.24)$$

$nl_1ml_2$  describes the electronic state of the two electrons, where  $n, m$  are the principle quantum numbers and  $l_1, l_2$  are the respective angular momentum quantum numbers.  $^{2S+1}L^\pi$  describes the symmetry of the whole system with total angular

## 2. Fundamental theory

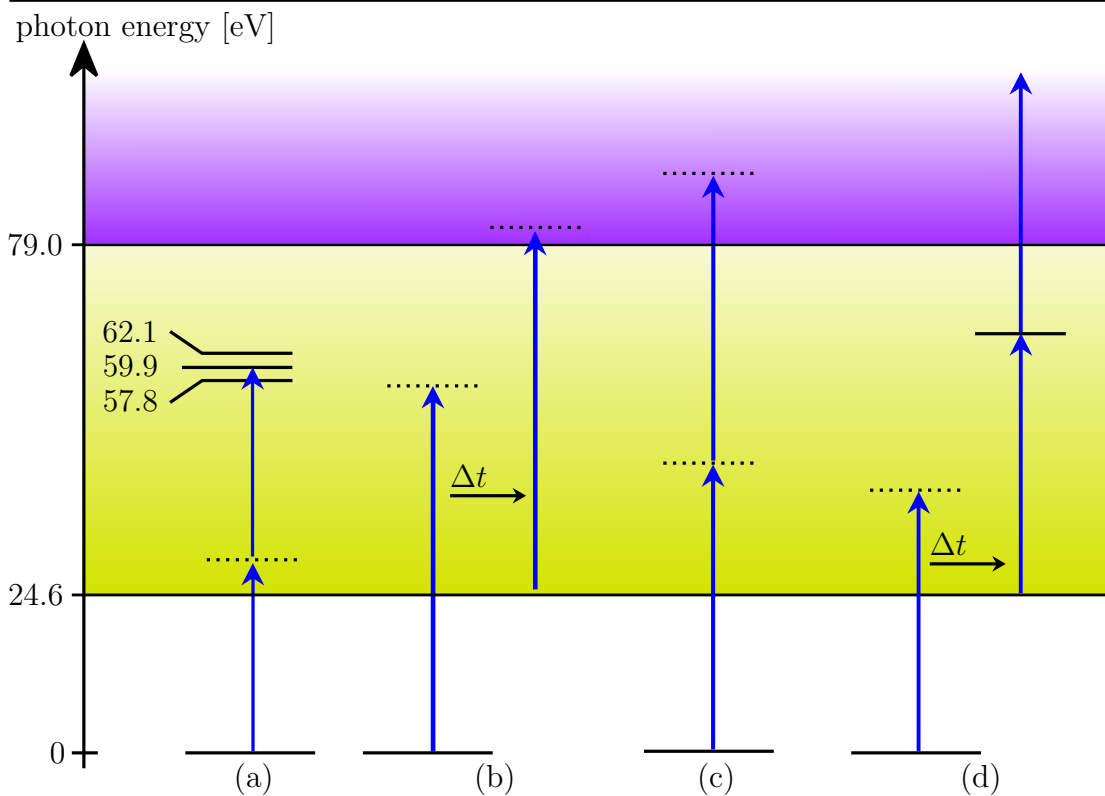


Figure 2.3: Overview over different processes and energy levels in helium. (a) The ATI with resonant doubly excited states. (b) Sequential two photon ionization. (c) direct two photon ionization. (d) sequential three photon ionization over helium ion resonance.

momentum  $L$  and the total spin  $S$ .  $\pi$  represents the parity, with  $o$  for odd and  $e$  for even.

The doubly excited state in study is  $2p2p\ ^1D^e$ . The ground state of helium ( $1s^2\ ^1S^e$ ) is even, therefore an even number of photon interactions is necessary to excite this state. A linear process is dipole forbidden to excite this state. Other doubly excited states close to the resonance are  $2s^2\ ^1S^e$  and  $2p2p\ ^1S^e$ . Energy and decay width has been calculated by Wang et al. and can be found in 2.1[4].

Furthermore, there is an odd photon doubly excited state in the vicinity. The well studied  $2s2p\ ^1P^o$  state has an resonance energy  $E = 60.15\text{ eV}$  and the decay width  $\Gamma = 37.6\text{ meV}$ [26]. The state can be linearly excited by a single photon.

In the photon energy domain between 40 eV and 57 eV there are no excited states in neutral helium. For the second experiment continuum dynamics are crucial. The TPDI differential cross-section has been the topic of many theory

## 2. Fundamental theory

${}_N(K, T)_n$	electron conf.	Symmetry	Energy	Decay width
${}_2(1, 0)_2$	$2s^2$	${}^1S^e$	57.835 eV	128 meV
${}_2(1, 0)_2$	$2p^2$	${}^1D^e$	59.908 eV	64.5 meV
${}_2(-1, 0)_2$	$2p^2$	${}^1S^e$	62.074 eV	6.42 meV

Table 2.1: Energy and decay width for the three doubly excited levels in the vicinity. Calculated by theory from ref. [4]. The first row gives the matching correlated quantum numbers.

calculations[13, 27–32]. Intuitively, we can anticipate the behavior. At an energy where TPDI just becomes possible, electrons will have a very small kinetic energy and have to share the energy 50:50. The reason is that if one of the electrons has more energy than the other, the slow electron will remain trapped in the atom’s potential. In addition, the slow electrons repel each other through the Coulomb interaction, so they always move in the opposite direction. The related phase-space is very small. Fermi’s golden rule gives us the relation  $\Gamma_{i \rightarrow f} \propto \rho(E_f)$ . For increasing photon energy, the phase-space grows quickly, as correlation plays a less important role. The quantum mechanically transition probability  $|\langle f | \hat{T} | i \rangle|^2$  remains comparably constant.

Singly ionized helium is hydrogen-like, therefore the resonance energies are given by the Rydberg formula:

$$\Delta E_{i \rightarrow f} = \frac{Z^2}{2} \left( \frac{1}{n_f^2} - \frac{1}{n_i^2} \right) \quad (2.25)$$

Those resonances are sharp and quite long-lived. They can be used as intermediate steps to further ionize the helium ion. The state most interesting for the following work is excited with 40.8 eV.

### 3 Experimental Setup

For experiments presented in this work, FLASH is the XUV light source. The REMI situated at the beamline FL26 is capable of measuring the three-dimensional momentum distribution of ionization and dissociation processes induced by the FEL pulses. In addition a new transient absorption spectroscopy beamline has been built to record the photon absorption spectra of the highly stochastic FEL pulses. The high frequency detector setup allows to record energy spectra for each pulse on a shot-to-shot basis while the FEL is in burst mode with a repetition rate of up to 100 kHz. The absorption target on the other hand gives many opportunities for future experiments. An overview over the whole beam path is given in Figure 3.1

The following chapter will cover the physics and functionality of the whole experimental setup. The last section §3.4 describes the calibration of the experimental setup using data from first commissioning measurements.

#### 3.1 Free electron laser physics at FLASH

FLASH is a source of XUV pulses with high brilliance. It uses accelerated electrons to produce synchrotron radiation in a coherent way. There are two separate undulator beamline namely FLASH1 and FLASH2. The experiment has been performed at FLASH2 to take advantage of the wavelength adaptability. This section will give an introduction about FEL physics, especially for the components of FLASH2.

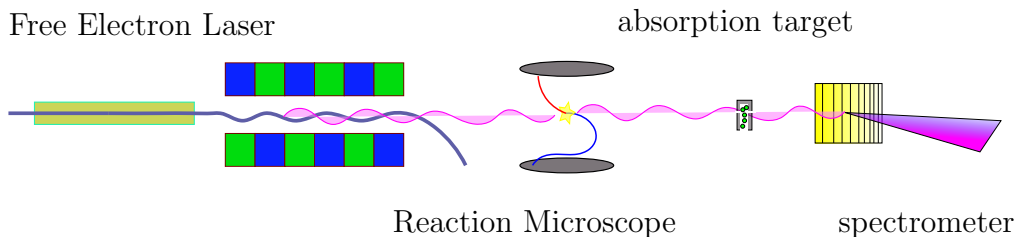


Figure 3.1: Overview over the experimental setup.

### 3. Experimental Setup

---

FLASH uses an RF-gun based photoinjector [33] as a high brilliance electron source. An electron bunch is created via a photocathode illuminated by an ultra-fast laser system. The electrons get picked up and are accelerated immediately by a pulse of the RF-gun. Multiple electron bunches can be accelerated at once with a single RF pulse, resulting in a so-called pulse train.

In a second step, the electrons are accelerated by multiple superconducting cavities. The strong repulsive force between electrons makes it impossible to form tight clusters prior to acceleration. Close to the speed of light, the Coulomb force in the lab frame weakens with  $1/\gamma^2$ , where  $\gamma$  is the Lorentz factor, such that tight bunching becomes feasible[1]. Between the accelerating structures, the bunch gets compressed multiple times via magnetic chicanes, forcing the faster electrons onto a longer path, such that the slower electrons can catch up.

The XUV radiation is then generated in an undulator. It consists of two sets of evenly spaced permanent magnets that force the electrons into a wiggly motion (c.f. Figure 3.1). The acceleration of electrons through the magnetic deflection causes the spontaneous emission of photons. The energy bandwidth of this stochastic emission is quite broad, while the central wavelength is described with [34]

$$\lambda_c = \lambda_u \frac{1 + K^2/2}{2\gamma^2}, \quad (3.1)$$

where  $\lambda_u$  is the length of a magnetic field oscillation given by the periodic arranged permanent magnets, and the dimensionless undulator strength  $K = \frac{eB_0\lambda_u}{m_e c 2\pi}$ , with the peak magnetic field  $B_0$ . FLASH2 is capable of changing the undulator gap. Therefore one can manipulate  $\lambda_u$  by moving the magnets and thereby tuning the central wavelength in an easy way.

The key for the FEL to produce high intensity pulses is similar to an optical LASER. The electrons have to interact coherently with the initial field produced by the initial spontaneous emission. While the electrons move close to speed of light, they travel along a longer trajectory as compared to the photons due to their wiggly motion. Therefore the electrons will always be slower than the photons they produce along their path through the undulator. The resonance condition for the electrons is that for every wiggly cycle they do, they are retarded by exactly one wavelength. In this way the electrons coherently interact with the

### 3. Experimental Setup

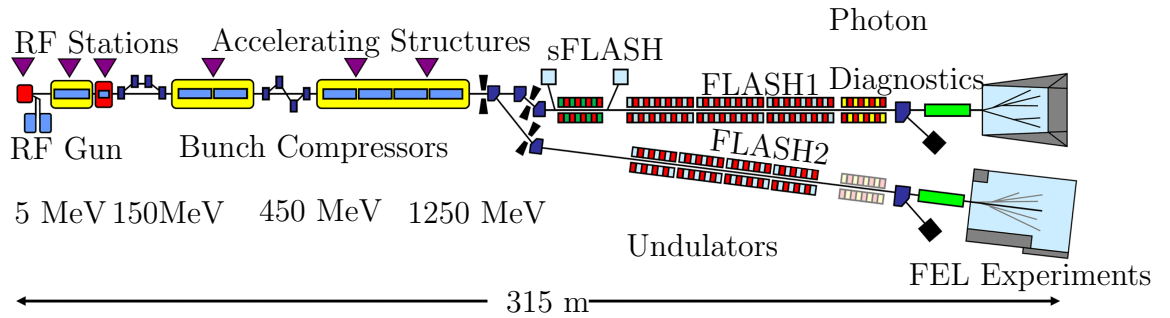


Figure 3.2: Schematic overview of FLASH(not to scale). The FLASH2 undulator was used with adjustable distances between the permanent magnets. Figure adapted from [1]

initial field.

The electron motion perpendicular to the beam direction  $v_{\perp}$  is either enhanced or decreased, dependent on the the electric field  $E$  pointing in the same direction or against it. The resonance condition implies that  $v_{\perp}$  and  $E$  either always point in the same direction or the opposite. Depending on the relative phase of the electrons to the initial electromagnetic field some electrons will accelerate, while others will decelerate. The electrons get compressed to so-called microbunches, separated by the resonant wavelength  $\lambda_{XUV}$ . In a static picture, the compressing force can be depicted by periodic potential wells traveling with the electron bunch (c.f. Figure 3.3). The electrons will lose energy by clustering in the minima of the potential and in doing so increase the electric field and therefore the depth of the periodic potential wells. This feedback loop results in an exponential growth of the field amplitude until saturation is reached or the undulator ends. This process is called **Self-Amplified Spontaneous Emission (SASE)**.

Resonance can also be met by all wavelengths  $\lambda_n = \lambda_1/n$  with  $n \in \mathbb{N}$  and  $\lambda_1$  being the fundamental wavelength. Careful derivations show that only odd values for  $n$  are inherently resonant[34]. However, due to off-axis electrons, the second harmonic  $\lambda_2 = \lambda_{XUV}/2$  can also play a significant role[36]. The FEL is tuned such that the central wavelength of the initial spontaneous radiation  $\lambda_c$  meets the fundamental resonance condition.

In reality the electrons span over a region much more spread out than the initial spontaneous photon. Spontaneous emission produced in different regions

### 3. Experimental Setup

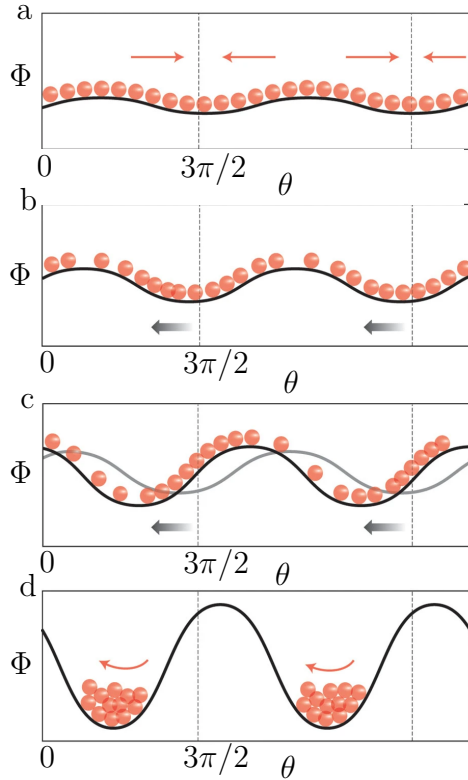


Figure 3.3: **(a)** The ponderomotive potential originating from the initial spontaneous emission exerts a force onto the electrons **(b)** The electrons move towards the potential wells, thereby losing energy and thus increase the radiation. **(c)** The bunching continues, while the electromagnetic field travels through the electron bunch. **(d)** Saturation is reached when all electrons are situated in the potential wells. Figure adapted from [35]

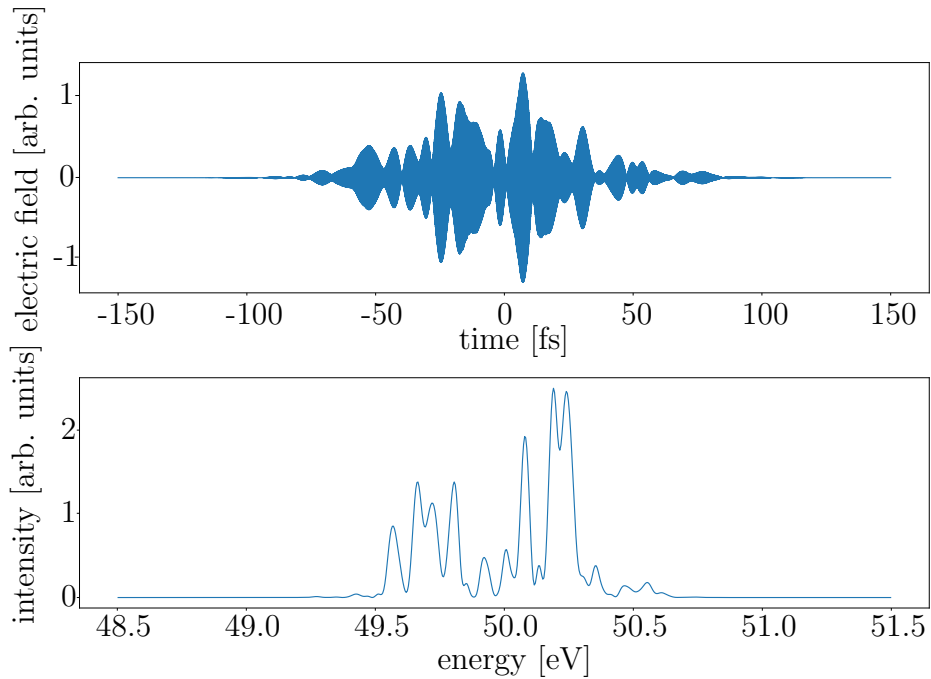


Figure 3.4: Pulse simulated with the Partial Coherence Method [37]. The pulse duration has been set to 50 fs and the bandwidth to one percent of the central wavelength.

of the electron bunch can get amplified independently of each other. This results in several sub-pulses with no phase correlation to each other. The individual sub-pulses themselves are coherent[35]. This behavior is called partial coherence. These pulses can be described via a stochastic random phase model called partial coherence method[37]. An exemplary pulse can be seen in Figure 3.4

The pulse's energetic width and pulse duration is well above the Fourier limit  $\Delta E \Delta \tau \geq \frac{\hbar}{2}$ . Usually we get  $\Delta E/E \sim 1\%$ . Also the pulses vary significant in intensity, pulse shape and duration on a shot-by-shot level.

FEL pulses which has been used for the presented work have central photon energies between 28 eV and 57 eV. The pulse energy follow a Poisson-distribution with the mean of  $\sim 8$  J. Pulse duration is measured with terahertz-field-driven streaking[38]. The pulse duration varies between  $<50$  fs to 300 fs.

## 3.2 Reaction Microscope

A **R**eaction **M**icroscope (REMI) is capable of measuring the momentum of multiple charged particles [2]. REMIs are used to investigate the reaction of atoms or molecules to radiation. In our case we measure the interaction of helium atoms with XUV pulses from the FEL. The REMI uses a homogeneous electric field to accelerate fragments of ionization onto large detectors. Measuring the **t**ime of **f**light (TOF) and the impact position, one can reconstruct the fragments initial momentum. A homogeneous magnetic field can be applied to make sure that even fast particles are captured with a full  $4\pi$  solid angle. The REMI used in this work is permanently situated at the beamline fl26 at FLASH2[39].

Helium atoms at room temperature have a mean kinetic energy of about 40 meV and subsequently a mean momentum of 4.5 au. The gas target has to be cooled to make the experiment feasible. Furthermore, the target density has to be low, such that space charge effects between ionization products are still negligible. Also due to detector design only few events can be measured. Low temperature and density is fulfilled by a supersonic molecular gas jet[41]. To further cool the target, the reservoir is cooled with liquid helium.

The FEL beam is focused into the supersonic gas jet in the center of the main



### 3. Experimental Setup

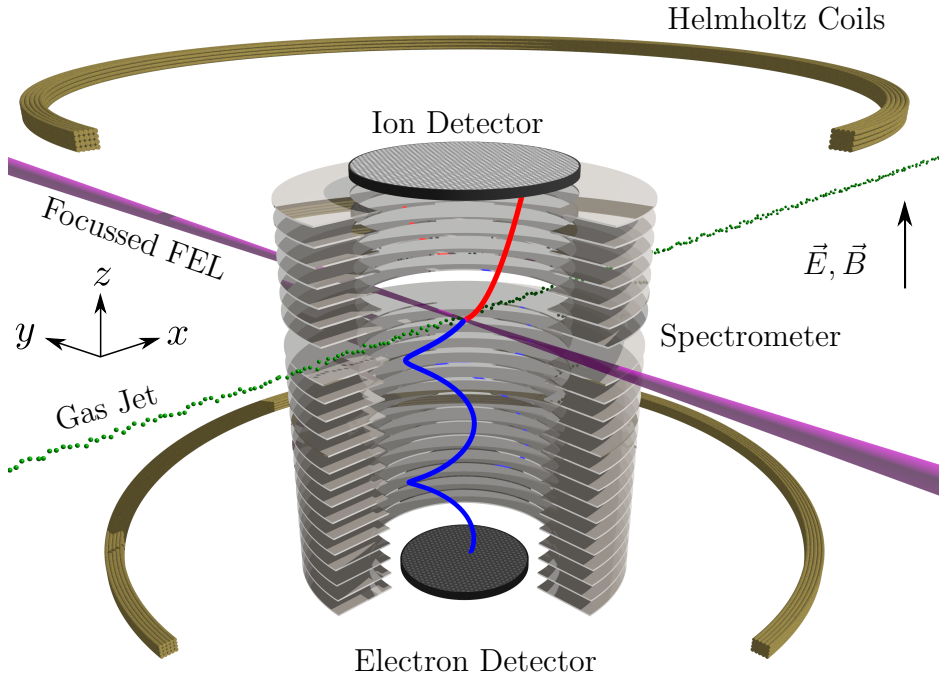


Figure 3.5: Illustration of the Reaction Microscope. Figure adapted from [40]

REMI chamber. The created ionization fragments are accelerated by a homogeneous electric field generated by 22 steel rings. They are coaxially arranged and separated by  $1k\Omega$  resistors to generate a constant potential gradient over the entire length of the chamber. Additionally, a magnetic field can be applied via Helmholtz coils. The magnetic field forces the charged particles onto a spiral path such that fast particles (especially electrons) do not collide with the walls but hit the detector. In this work, electrons were not measured and therefore no magnetic field was applied.

Directly in front of the detectors, two fine metal grids are installed. A high voltage is applied between the grid and the detector to accelerate the particles briefly in order to increase detection efficiency.

The detectors themselves consist of micro-channel plates (MCPs) [43] and delay-line anodes [44] (c.f. Figure 3.6). MCPs are plates with holes arranged in a grid. The inner walls are coated with a material with a low electron work function (e.g. GaP). This allows the highly accelerated ion to launch an electron avalanche. A voltage is applied between the front and back of the MCP such that the avalanche causes a voltage drop which can be measured. This signal together with the trig-

### 3. Experimental Setup

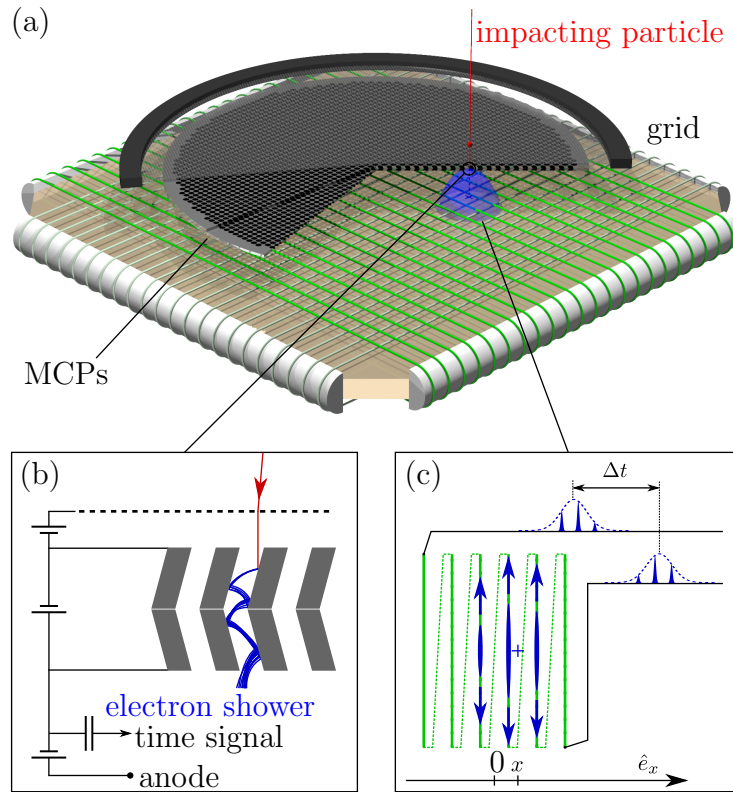


Figure 3.6: (a) Illustration of time- and position detector. (b) The impacting particle releases an electron avalanche in one of the channels of the MCP. The drop in voltage is used as the time signal. (c) The electron avalanche hits the positive charged wire grid and produces a signal traveling to both ends of each wire grid. From Ref. [42]

ger signal of the FEL is used to measure the TOF.

The delay-line anodes consist of long cooper wire wound around an insulator in a parallel manner. The ion detector uses two perpendicularly aligned lines, while the electron detector uses three. The wires are put at a positive voltage. The electron avalanche of the MCP will be attracted by the wire and drop the voltage in the impact vicinity. This signal will travel in both directions perpendicular to the winding at constant velocity  $v_{\perp}$ . The arrival times at both ends of the wire can then be used to reconstruct the position of the initial signal.

$$x = \frac{v_{\perp}}{2} (t_1 - t_2) \quad (3.2)$$

Finally, the position information and the TOF can be used to reconstruct the three dimensional initial momentum of the particle. Further information on the reconstruction of momenta can be found in the appendix§7.1.

A disadvantage of this measurement method is that the position of two particles arriving on the detector at similar times cannot necessarily be distinguished. If the signals of the delay lines overlap, the position cannot be uniquely assigned. Especially when measuring fast electrons this implies that only a few particles should be ionized within each laser pulse. The constraint is not as strict for ions, as they are slower, such that individual impact events are more separated in time. In addition, measuring electrons and ions in coincidence is only applicable for few ionization events per shot. The nonlinear effect we measured is highly unlikely such that a higher detection rate proved to be necessary. Therefore we measured ions only.

### 3.3 Absorption spectroscopy beamline

Replacing the previous beam dump, we installed a beamline for transient absorption spectroscopy. The absorption beamline can either act as a diagnostic tool for the REMI spectrometer, measuring the SASE spectrum of the FEL on a shot-to-shot basis, or it can be used to perform transient absorption spectroscopy measurements. Therefore, a gas target is installed in the absorption beamline.

For the experimental work done during this thesis, the absorption target was only used to calibrate the spectrometer. Other work done with a similar setup shows the power of this experimental scheme[45–50].

The new beamline is interlocked with the REMI to allow for undisturbed propagation of the FEL beam. It is necessary to retain an ultra-high vacuum in the REMI of about  $2 \times 10^{-11}$  mBar to suppress detector hits stemming from the interaction of the FEL with residual background gas. Therefore several small chambers are used for differential pumping between the absorption target and the REMI.

The first of three main chambers after the REMI contains the refocusing mirror. It is a toroidal mirror, built from a silicon single-crystal with a  $\sim 30$  nm XUV-reflecting nickel coating. With a focus length  $f = 60\text{cm}$ , the mirror is used in a 2f-2f configuration to image the FEL focus of the REMI into the gas absorption target. The mirror can be aligned using actuators for pitch, roll and

### 3. Experimental Setup

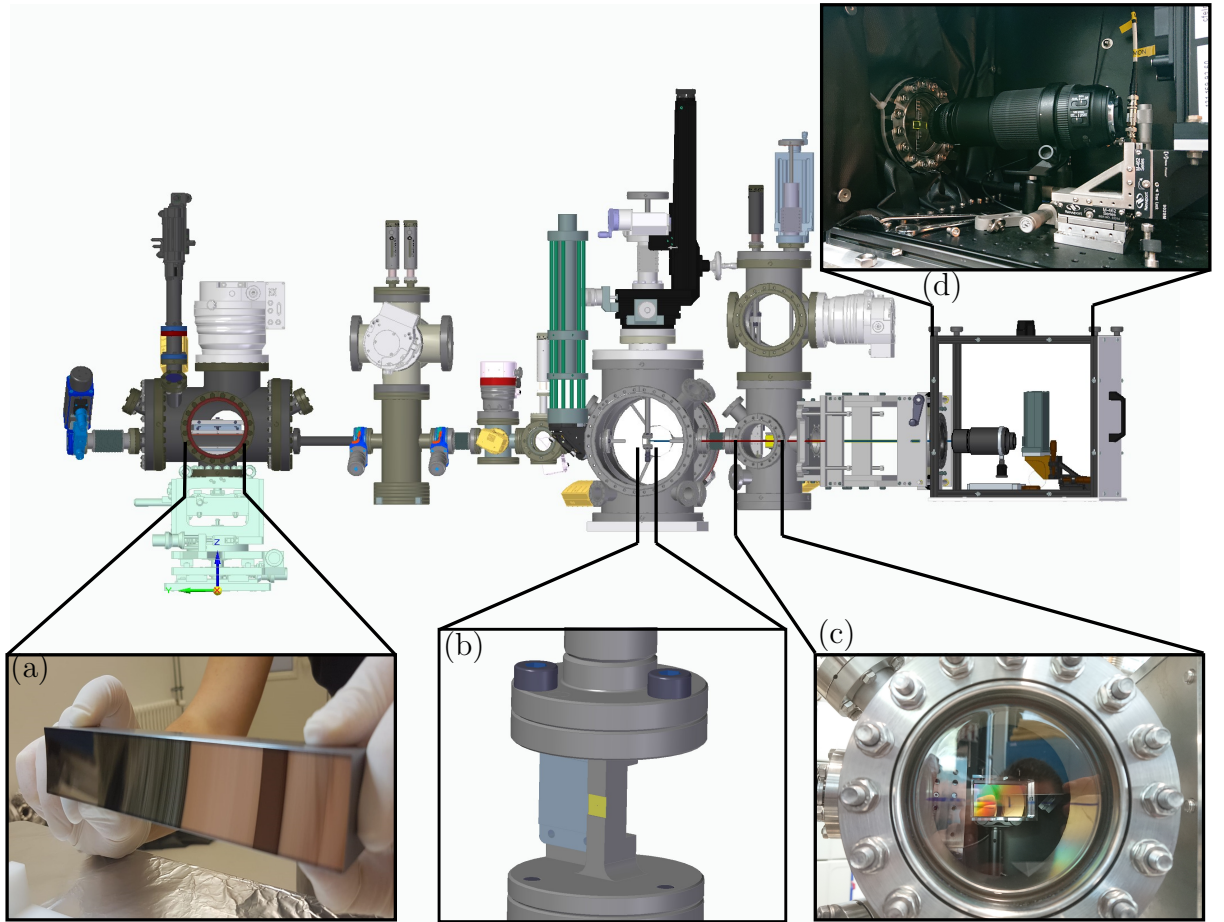


Figure 3.7: Overview of the absorption spectroscopy beamline. The beam comes from the left. (a) Toroidal mirror to refocus XUV-beam into target chamber. (b) Target with a small hole. Gas flows from the bottom and it can be steered from the top. (c) Grating chamber with concave refocusing variable-line-space grating. (d) Optical setup with small YAG:Ce crystal illuminated by XUV spectra, camera lenses for imaging and the GOTTHARD detector.

yaw movements, as well as translation of the whole mirror chamber along all three axes.

The target cell is a tube of 2 mm inner diameter with two 100  $\mu\text{m}$  diameter holes as entrance and exit for the focused beam. It can be steered with an external manipulator along all three axes, as well as turned along the cell's axis. The absorption target can be operated with backing pressures of several hundred millibars. In principle parallel operation with the REMI is possible.

The focus of the FEL also acts as the entrance slit for the wavelength spectrometer. The grating itself is a concave variable-line-spacing grating (VLS) with

### 3. Experimental Setup

---

flat-field image focusing[51]. It is suited for wavelengths between 22nm to 124nm.

The concave grating refocuses the individual wavelengths onto a crystal made of yttrium aluminum garnet activated by cerium (YAG:Ce). The YAG:Ce crystal, when illuminated by XUV light, fluoresces at a wavelength of  $\sim 550$  nm and has a fast decay constant of 70 ns[52]. The emitted fluorescence can then be detected outside of the vacuum, which enables easy access and the use of detectors that are not vacuum compatible.

We used an optical setup made out of two commercially available camera lenses in the so-called tandem-configuration. The first camera lens collimates the light, while the second lens focuses the light onto the detector. One can achieve a magnification with different focal lengths  $M = \frac{f_2}{f_1}$ , where  $f_1$  and  $f_2$  are the focal lengths of the first and second camera lenses. Different configurations of camera lenses allow for a quick change of magnification.

The setup used for the experiments was the Nikon AF-NIKKOR 24mm f/2.8 D in the front and Nikon AF-S 70-300mm f/4.5-5.6 VR in the back. The second camera lens being a zoom objective allowed for quick changes in magnification. For the experiments described in this work a magnification of  $\sim 12$  was used.

The optical system projects the fluorescent light of the YAG:Ce crystal onto the **Gain Optimized microTrip sysTem with Analog ReaDout** (GOTTARD) detector [53, 54]. It is a one-dimensional silicon strip sensor allowing frame rates higher than 1 MHz. The fast detector allows for the detection of spectra on a shot-to-shot basis in the burst mode of the FEL. Individual strips/pixels of the detector are  $50 \mu\text{m}$  spaced out. With a magnification of 12 the effective pixel size projected onto the crystal is only  $4.2 \mu\text{m}$ . In the interesting energy domain this corresponds to a resolution of  $\sim 2.4$  meV.

## 3.4 Commissioning measurements

In the following section preliminary results are presented that are used to calibrate the transient absorption beamline. Argon gas was used in the absorption target cell for the energy calibration of the spectrometer. In the last part a correlation between the pulse energy measured via the integrated counts detected in the

photon spectrometer and detector hits in the REMI is used to guarantee measured consistency between both apparatuses.

### 3.4.1 Energy calibration

A calibration for the wavelength spectrometer was done for the energy window between 27.5 eV and 30.5 eV. We measured the  $3s^23p^6\ ^1S \rightarrow 3s3p^6np\ ^1P$  window resonances in Argon[55]. Those are autoionization resonances (for more information c.f. §2.3.2), where the two paths into continuum interfere destructively such that the cross section significantly drops on the resonance(c.f. Figure 3.8). This results in an increase in transmission through the gas sample at the position of the resonances.

We scanned the FEL-wavelength via the movable undulators and detected the transmission signal. The absorption resonances with  $n = 5, 6$  and  $7$  are well recognizable (c.f. Figure 3.10).

We fitted the individual resonances with fano-lineshape curves (eq:(2.22)). The resolution of the spectrometer has been accounted for by convolution with a Gaussian kernel.

The  $n = 5$  resonance has been fitted with a fixed decay width  $\Gamma = 25$  meV known from the literature [55]. As intensity is comparably low, we assume the rest of the broadening to arise from the finite resolution of our spectrometer. The fit results in a resolution of 33.2 meV. The other resonances were fitted with the same spectrometer resolution as determined above. Additional line broadening due to the high intensity of the FEL radiation can be observed. The further investigation of these effects is beyond the scope of this work. Finally, a linear regression using the pixel position of the resonances were used to energy calibrate the spectra (c.f. Figure 3.9).

### 3.4.2 Determination of spectral resolution

Multiple effects influence the energy resolution of the spectrometer. Only the major contributing factors will be discussed here.

### 3. Experimental Setup

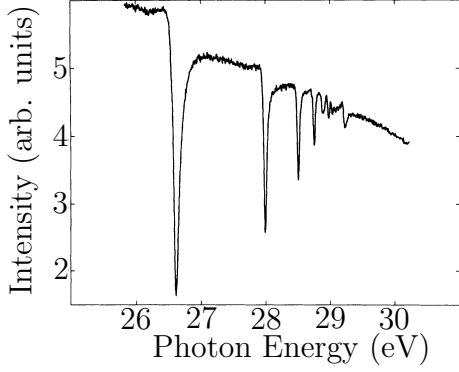


Figure 3.8:  $\text{Ar}^+$  yield measured by Sorensen et al.[55]

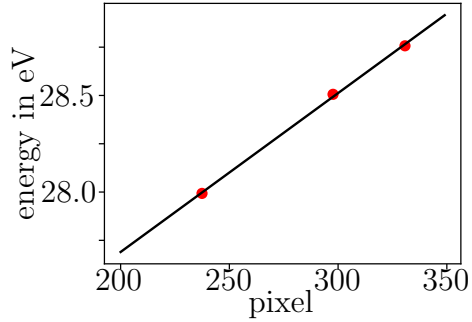


Figure 3.9: linear fit through measured resonances compared to literature values for the energy.

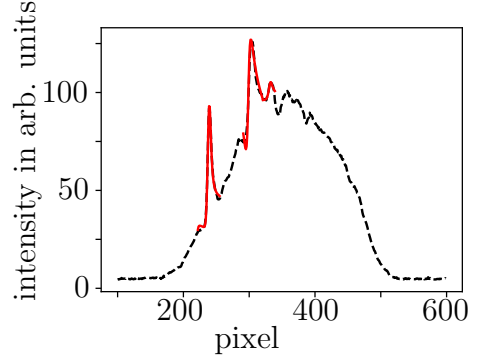


Figure 3.10: Mean spectra with fano line-shape fits for the  $n = 5, 6$  and  $7$  resonances.

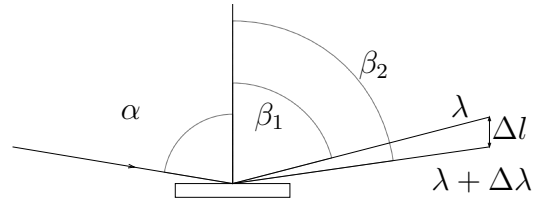


Figure 3.11: Illustration of grating equation.

The resolution of a standard grating with evenly-spaced grooves is given by:

$$R = \frac{\lambda}{\Delta\lambda} = mN \quad (3.3)$$

with  $\lambda$  the central wavelength,  $N$  the number of grooves illuminated and  $m$  the order of diffraction. To first order, this equation also holds for a variable line-spacing grating. Higher-order effects are negligible for the treatment in this work.

The diffraction angles are governed by the grating equation:

$$\sin \alpha - \sin \beta = \frac{m\lambda}{d} \quad (3.4)$$

where  $\alpha$  is the incident,  $\beta$  the reflected angle and  $d$  is the spacing of the grooves.

With (3.4) we can determine the linear displacement on the YAG:Ce screen  $\Delta l$  per  $\Delta\lambda$ :

$$\frac{\Delta l}{\Delta\lambda} = \frac{rm}{d} \frac{1}{\sin^2 \beta \sqrt{1 - \sin^2 \beta}} \Big|_{\sin \beta = \frac{m\lambda}{d} - \sin \alpha} \quad (3.5)$$

### 3. Experimental Setup

	$\Delta\lambda$	$\Delta l$	$R = \frac{\lambda}{\Delta\lambda}$	$\Delta E$
Grating	2.29fm	2.90 $\mu\text{m}$	18000	1.67meV
Pixel	3.29fm	4.17 $\mu\text{m}$	12536	2.40meV
Focus	19.8fm	25.0 $\mu\text{m}$	2089	14.4meV
Measurement	52.5fm	66.4 $\mu\text{m}$	843	33.2meV

Table 3.1: Resolution approximation of different factors.

where  $r$  is the distance between grating and spectral plane. The angles and displacements are illustrated in Figure 3.11.

The optical lenses in front of our detector create a 12-fold magnification. A single pixel of 50  $\mu\text{m}$  width corresponds to a 4.2  $\mu\text{m}$  spot on the YAG:Ce screen. Using (3.5), we can approximate the resolution loss due to the discrete pixels.

A major broadening of resolution is introduced by the finite size of the spectrometer entrance slit which, in our case, is given by the focus size. We are not able to reach the diffraction limit for our mirrors. With the data available on the focus size within the REMI[39, 40], we estimate the focus size in our target chamber to be  $\sim 25 \mu\text{m}$ .

For the parameters of our grating (Hitachi #001-0639), a central wavelength of 41.2nm and assuming at least 60% of grooves illuminated, the estimated contributions on line broadening are listed in table 3.1. Further information on the measured resolution can be found in §3.4.1.

Compared to previous measurements, the resolution is of the same order. A quite similar setup at FLASH[50] achieved 65.9meV. For this measurement a separate 2D-entrance slit was used instead of relying on the focus, which could explain the deviation.

#### 3.4.3 REMI-Spectrometer correlation

During the commissioning of the experimental setup, we were able to measure first correlations between REMI events and wavelength spectra.

The major interaction between the XUV-pulse and the target gas through photoionization is described by the first order rate equation (2.8). Assuming only



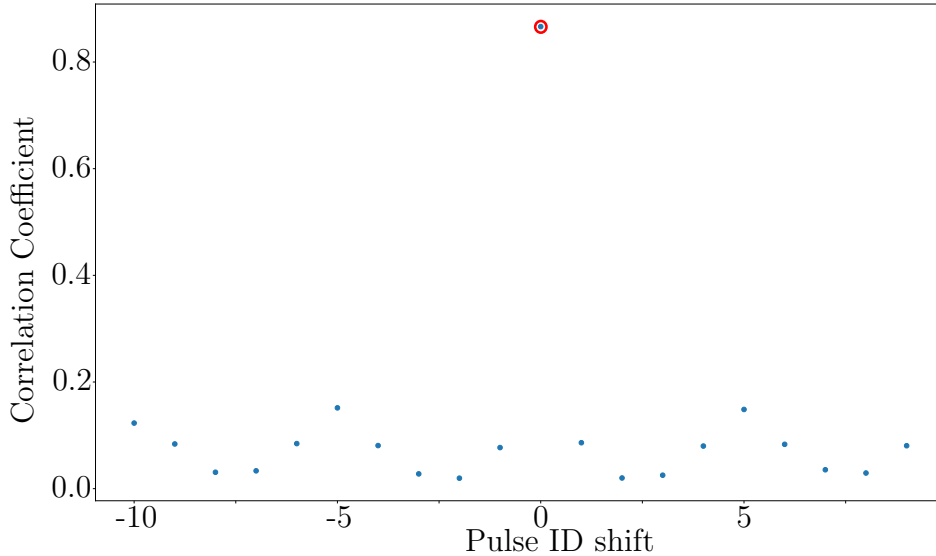


Figure 3.12: Spearman correlation coefficients for different Pulse ID shifts. Highest correlation coefficient marked with red circle. In this example no correction was necessary. More information in the text

first order processes, the number of generated ions is proportional to the pulse energy  $E$ . The spectrally integrated counts detected in the photon spectrometer are used as a measure for the incident pulse energy. This is true since the dilute gas target in the REMI does not significantly alter the transmitted spectra. The spectrometer counts are then correlated with the total number of events measured in the REMI for every FEL shot.

The number of events in the REMI is usually only between zero and four per shot. To avoid stochastic fluctuations, we sum both pulse energy and events for an entire pulse train. We use the Spearman coefficient to quantify a correlation between the pulse energy and REMI detector hits.

REMI and GOTTHARD data are recorded by separate data acquisition systems. Both of these systems store the Pulse-ID as a unique identifier for every pulse train. Past measurements have shown the possibility of a Pulse-ID shift, meaning the stored Pulse-ID can be shifted by an integer number. For all measurement series analyzed, the correlation was calculated for multiple Pulse-ID shifts (c.f. Figure 3.12). The correlation coefficient shows an unique mapping. The Pulse-ID shift observed is between minus one and one.

# 4 Above Threshold Ionization in Helium

Two experiments using the presented setup were conducted during this thesis. The first experiment concerns itself with a two-photon above-threshold ionization (ATI) resonantly enhanced by an autoionizing state. The quasi-bound resonant state in the single electron continuum increases the cross-section for the two-photon process by several orders of magnitudes [4]. This process is probing the electron-electron-nucleus interaction in a quasi-bound system and therefore investigates one of the most fundamental non-perturbative light-matter interactions.

Two-photon absorption allows us to excite states with even symmetry from the ground state. We use 30 eV photons to doubly excite the  $1S^e 1s^2$  ground state transition into  $1D^e 2p^2$  at 59.9 eV (for more information see §2.4). The REMI measures the ion momentum, which in turn is equivalent to the electron momentum due to momentum conservation. The absorption spectroscopy beamline measures the wavelength spectra for each individual event. Both measurements are to be combined to classify the resonance.

The current chapter starts with numerical calculations and estimations in section §4.1. Section §4.2 talks about the experiment itself and presents first results. Finally, the section §4.3 gives a discussion and outlook for the presented data.

## 4.1 Numerical calculations

The theoretical cross-section of the two-photon process has been calculated ab-initio by Wang and Greene[4]. They used multichannel quantum defect theory together with a streamlined R-matrix method.

The provided cross-section was used in this work to make two further numerical simulations. A rate equation model is used to explore the experimental

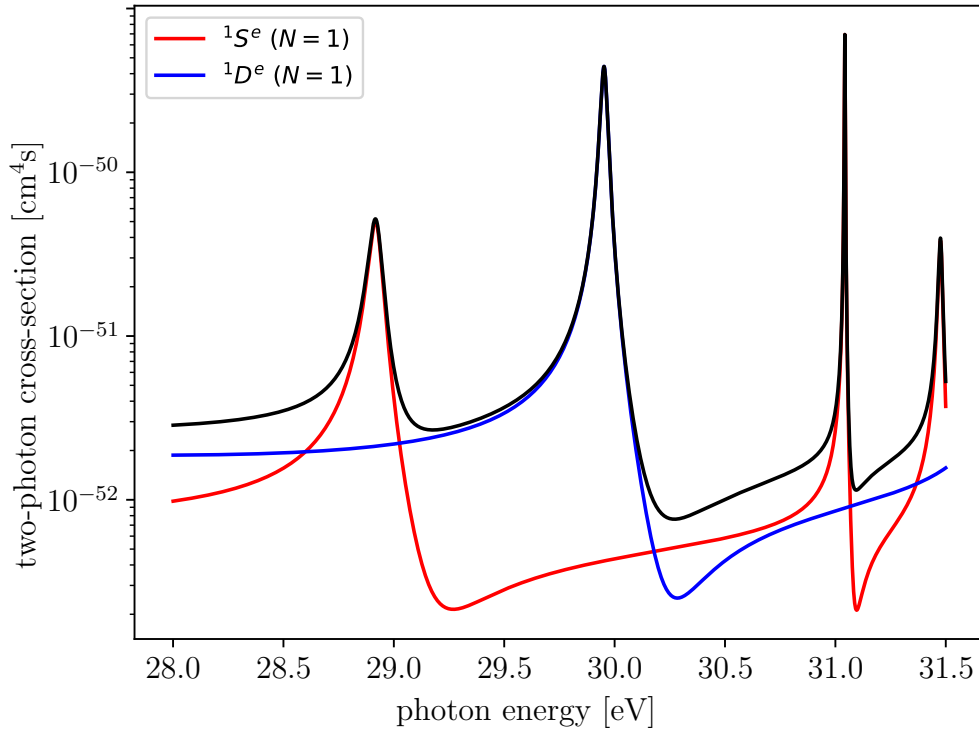


Figure 4.1: Two-photon differential cross-section calculated by Wang et al.[4]. The red and blue line show the partial cross-section for the  $1S^e$  and  $1D^e$  symmetry. The black line shows the total differential cross-section.

parameter space and observe scaling with pulse energy. The few-level model simulates the quantum mechanical behavior of the two-photon resonance and is as proof of principle for correlation methods between the incident FEL spectra with measured ions.

#### 4.1.1 Rate equations

We use both rate equations, eq.(2.8) and eq.(2.10), to estimate the individual populations of the linear and the nonlinear process. The simulation takes a spatially extended pulse into account. The rates for each point in space are calculated separately. Assuming cylindrical symmetry, with constant intensity along the beam direction and a Gaussian distribution perpendicular to it. For simplicity Gaussian pulses with a pulse duration of 50 fs are used instead of the stochastic FEL pulses. This will give us the required estimate on expected count rates. The preliminary estimation has been important to choose sensible FEL

#### 4. Above Threshold Ionization in Helium

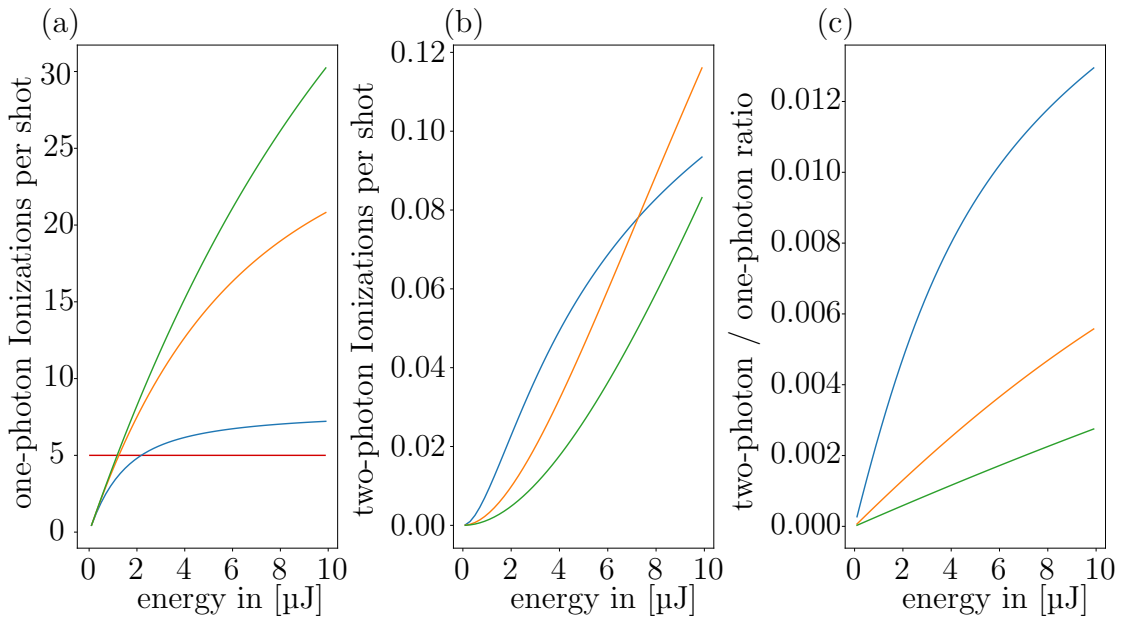


Figure 4.2: Rate equation solved for the parameters discussed in main text. The blue, orange and green curve are the solutions for different focus spot sizes of 10  $\mu\text{m}$ , 20  $\mu\text{m}$  and 30  $\mu\text{m}$ , respectively. (a) The number of single photon ionizations per shot induced by the linear process. (b) The probability of a two-photon process happening per laser shot. (c) The ratio between the nonlinear and trivial linear process.

pulse parameters for the experiment. Given too much pulse energy, we will have too many events and the REMI will not be able to detect individual events. If we do not have enough intensity, the nonlinear effect will be highly suppressed compared to the linear process.

The available energy  $E$  of a pulse can be calculated given the intensity  $I(t, \mathbf{r})$ :

$$E = \int dt d\mathbf{r} I(t, \mathbf{r}) \quad (4.1)$$

with the integration over the time axis and the area perpendicular to the beam-direction. Reverse engineering, we can simulate pulses with a defined energy, which can then be input into the rate equation. The pulse energy compared to the intensity is an experimental parameter that can be measured[56].

We assume an interaction volume given by a cylinder with the base area given by the focal spot size and the length given by the spatial extension of the gas jet ( $\sim 1$  mm). The particle density in the jet is on the order  $\sim 1 \times 10^9$  particles/ $\text{cm}^3$ [57]. If approximately more than five particles hit the detector at the same time, we are not able to correctly assign each particle to their TOF and position. At the

same time, a low ion number is desired because the repulsion of the individual ions due to Coulomb interaction among each other interferes with the momentum resolution (see also §4.2.2).

In Figure 4.2 the simulation results for different focal spot sizes are presented. For small pulse energies, the probability for a one-photon process increases linearly with the pulse energy, while the probability for the two-photon process increases quadratically. The signature of this scaling becomes clear in the linear increasing ratio. For higher pulse energies a depletion effect is visible. Especially for a smaller focal spot size, the depletion effect is increased as fewer atoms are available in the smaller volume while the intensity in this volume is comparatively higher. The red line in the left panel marks five particles, which is the maximal amount of particles desired to be measured by the detection scheme.

### 4.1.2 Few-level simulation

While the rate equations give us an estimate about the expected count rates, it does not take the actual physics into account. Instead, the quantum mechanical behavior of helium is described by a few-level system. With the stochastic FEL pulses obtained from the partial-coherence model[37], the experimental conditions are well described. Pulses simulated by the partial coherent method behave similarly to advanced ab-initio simulations[58], but have low computational cost in comparison. The subsequent section describes the toy system and discusses new techniques to gather information with the data available during the experiment.

The simulated few-level atom evolves under the constraints of the free Hamiltonian  $\mathcal{H}_0$  and the interaction Hamiltonian with an electric field  $\mathcal{H}_I(t)$ .  $\mathcal{H}_0$  is constant in time and the time dependence of  $\mathcal{H}_I$  can be separated:  $\mathcal{H}_I = \varepsilon(t)h_I$ .

$$\mathcal{H}_0 = \begin{bmatrix} E_0 & 0 & 0 & 0 \\ 0 & E_c & 0 & 0 \\ 0 & 0 & E_{c^*} & V \\ 0 & 0 & V & E_e \end{bmatrix}, h_I = \begin{bmatrix} 0 & d_{0-c} & 0 & 0 \\ d_{0-c}^* & 0 & d_{c-c^*} & d_{c-e} \\ 0 & d_{c-c^*}^* & 0 & 0 \\ 0 & d_{c-e}^* & 0 & 0 \end{bmatrix} \quad (4.2)$$

With the populations available by the rate equations, we hand-tune a few-level system to behave like a helium atom in the particular energy regime (see appendix §7.2).

We simulate electric fields of FEL pulses with the partial coherence method[37] constrained with a fixed pulse energy. We apply the split-step algorithm (§7.3) to calculate the interaction with the four-level system. The non-linear process is reflected in the population which is lost into the two-photon continuum. This corresponds to the probability that the electron is ionized by the two-photon process. The population loss can be computed for every time step as follows:

$$\mathcal{L}(t_n) = p_{c^*}(t_n) \left(1 - e^{-\Gamma \Delta t}\right), \quad (4.3)$$

where  $p_{c^*} = |a_{c^*}|^2$  is the population in the second continuum channel with energy  $E_{c^*}$ . The sum over all time-steps of the pulse can then be interpreted as the total contribution of the two-photon ionization.

The simulated data is used to test and verify techniques to reconstruct the line-shape of the differential cross-section. The FEL energy bandwidth is large compared to the resonance line width. Therefore, a simple scan using the central wavelength does not suffice to resolve the resonance. Instead, one can use the individual spikes created by the stochastic process to increase the energy resolution to sub-bandwidth.

The resonance is not excited by a linear process, but a two-photon process. The fundamental FEL spectrum does not represent the spectrum of interest for the two-photon process, as illustrated by the following thought experiment: The atom with its narrow resonance is excited by two photons with a total energy of  $2 \times 30 \text{ eV} = 60 \text{ eV}$ . The hypothetical FEL pulse has two spikes in the energy spectrum at 29 eV and 31 eV. The fundamental spectra suggests both spikes being off-resonant. Nevertheless, the atom is excited perfectly on resonance by the sum of the 29 eV and the 31 eV photons. Considering this effect, the relevant physical quantity is the non-normalized autocorrelation of both fields  $\tilde{I}(2\omega)$ :

$$\tilde{I}(2\omega) = \left| \int d\Delta\omega \varepsilon(\omega + \Delta\omega) \varepsilon(\omega - \Delta\omega) \right|^2 \quad (4.4)$$

where  $\varepsilon(\omega)$  is the electric field in the frequency domain. In the following this will be called the true two-photon spectrum.

In the actual experiment there is no access to the phase information of the pulse. Instead, the absorption beamline is used to measure the intensity spectrum  $I(\omega) = |\varepsilon(\omega)|^2$ . The phase, and therefore, the time information is lost. Using

the available data, the comparable quantity is a self-convolution to mimic the two-photon spectra:

$$\hat{I}(2\omega) = \int d\Delta\omega I(\omega + \Delta\omega) I(\omega - \Delta\omega) \quad (4.5)$$

The self-convolution is equal to the two-photon spectrum (4.4) if the phase of the pulse is flat, which is not expected for partial coherent FEL pulses. A flat phase is equivalent to a pulse where all wavelengths are available during the whole pulse duration. FEL pulse can have a temporal chirp, which leads to some frequencies only arriving at the beginning of the pulse, while other frequencies only appear at the end.

FEL spectra feature several spikes (c.f. Figure 3.4). Sorting the spectra for the position of the highest spike results in a pseudo-scan through the entire bandwidth of the FEL. With this scan, we can in principle, recover the form of the two-photon resonance with a resolution only limited by the width of the narrow spikes. The width of the spike is close to the Heisenberg limit  $\Delta E \cdot \Delta\tau \geq 2\pi$ .

For the described purpose, 10 000 pulses are simulated with a central photon energy of 30 eV, a bandwidth of 300 meV and a pulse length of 75 fs. For each pulse, the toy model is solved and the energy spectra are sorted as described above. Figure 4.3 shows the result using either the fundamental spectra, the self-convoluted spectra (4.5) or the true two-photon spectra (4.4). Sorting for the fundamental spectra reveals the resonance with a resolution similar to the bandwidth of the pulses. However, using the true two-photon spectra, the resonance is revealed with much higher resolution. Finally, sorting for the convoluted spectra images the resonance with a resolution of about a third of the pulse's bandwidth. In conclusion, the method of self-convoluting the spectra improves the resolution to values better than the bandwidth of the pulse itself.

Another way of correlating spectra with the corresponding solutions of the toy model is a mock-covariance correlation function:

$$S(I(\omega), p) = \langle I(\omega) \cdot p \rangle - \langle I(\omega) \rangle \langle p \rangle. \quad (4.6)$$

$\langle \rangle$  is the mean over all pulses and  $p$  is the probability of the two-photon ionization event being measured. For  $I(\omega)$  we can use the three different calculated spectra as discussed above.

#### 4. Above Threshold Ionization in Helium

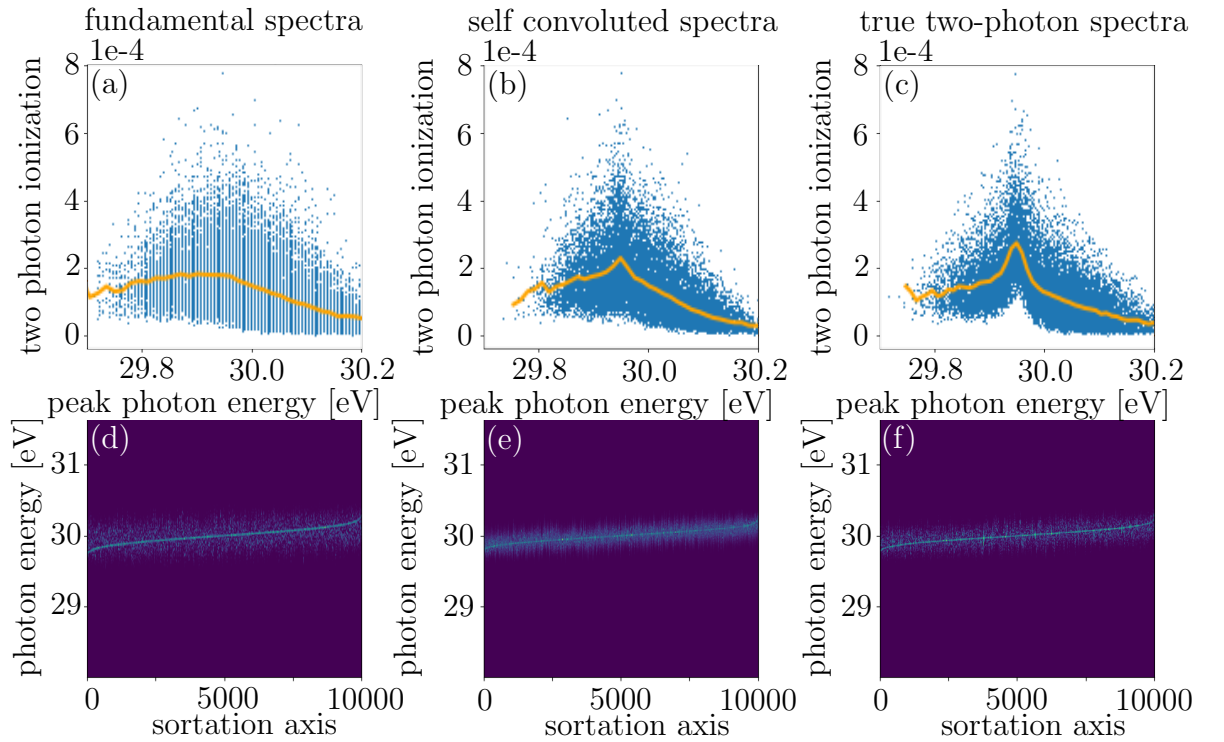


Figure 4.3: Pseudo photon energy scan, by sorting for the highest peak in the photon spectra. Upper panels (a-c) shows the result of the scan. Individual pulses and the resulting probability for a two-photon ionization are assigned to their respective photon energy peak in blue. The orange curve shows an moving average. (e-f) The individual spectra on the y-axis sorted with respect to the position of the maximal peak in order to depict the pseudo scan. (a,d) depicts the result using the fundamental spectra, (b,e) uses the self-convoluted spectra and (c,f) uses the true two-photon spectra.

In Figure 4.4 the correlation function for the different calculated spectra is shown. All curves are normalized to their maximum value for easier comparison of the width and shape. The vertical red line depicts the maximum cross-section of the initial resonance. The positive parts can be interpreted as an increase in cross-section due to the Fano resonance, while the negative values correspond to a decreased cross-section. Zero contribution is caused by the non-resonant background absorption. For all spectra, the general form of the resonance is reproduced. The difference of using the three different calculated spectra is apparent in the width of the resulting resonance. Using the true two-photon spectra results in a sharp peak close to the actual resonance with a resolution given by the individual spikes in the partially coherent spectra. The convoluted spectra



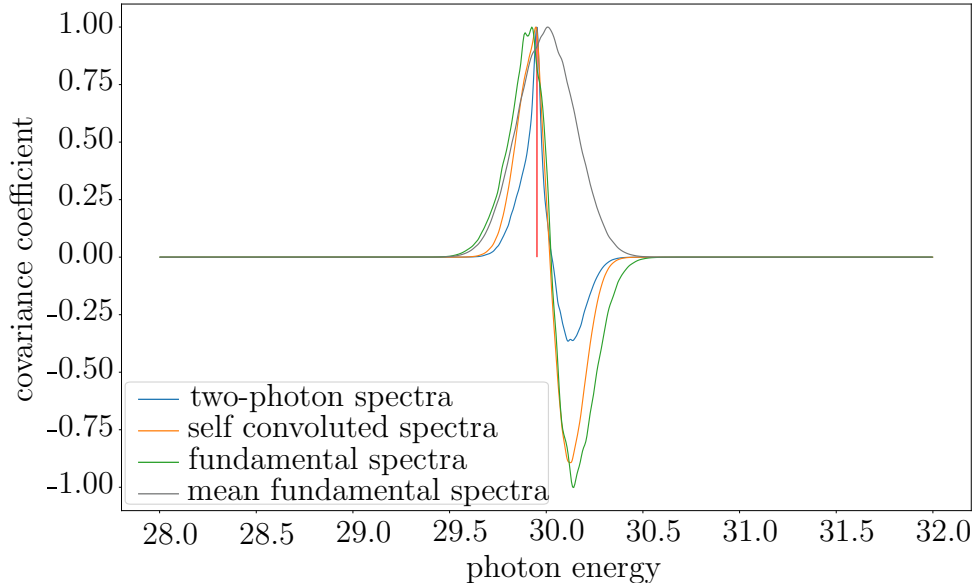


Figure 4.4: Calculated mock-covariance correlation function. The different colors show the function calculated with the three different calculated spectra. All functions are normalized to their maximum value for better comparison.

perform better than the fundamental spectra and shows the actual peak of the resonance close to the correct photon energy.

In conclusion, correlating broad photon energy spectra with nonlinear events should be done by using the true two-photon spectra. We have shown that the self-convoluted spectrum mimics the two-photon spectrum well enough to increase the resolution below the bandwidth of the FEL.

## 4.2 Experiment

The first experiment was performed with the FEL tuned to a central photon energy of 29.9 eV. The pulse energy, averaged over an entire FEL bunch train, is measured by a gas monitor detector (GMD) before entering the experimental hall[56]. The pulse energy follows a broad distribution (c.f. Figure 4.5). After the GMD multiple apertures, filters and mirrors attenuate the pulses, therefore the integrated GOTTHARD spectra are used as a measure of pulse energy for the following discussions. The broad pulse energy distribution is used to perform de-facto pulse energy scans by sorting the FEL shots and the corresponding measured

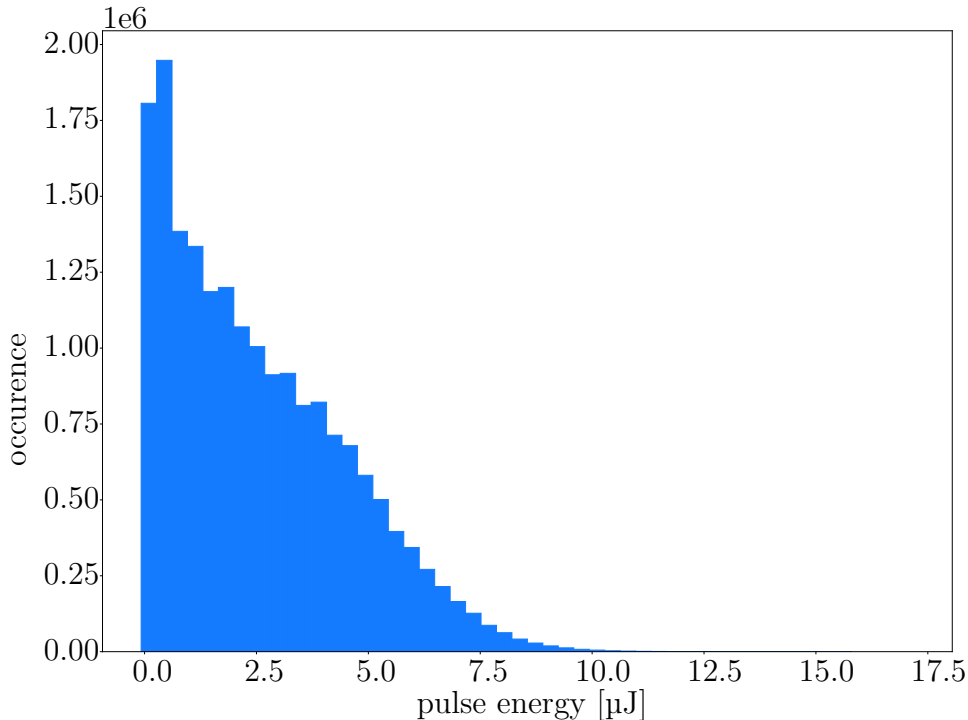


Figure 4.5: The pulse energy varies between individual shots. The broad variation allows to have an intrinsic intensity scan without varying external parameters.

events according to their respective pulse energies.

Compared to the linear process, the two-photon process is about three orders of magnitudes less likely. At the same time, we can expect the intensity of the second harmonic of the FEL at  $\sim 60$  eV to be about three orders of magnitudes smaller than the fundamental wavelength[59]. The ionization with the second harmonic is enhanced by the  $2s2p\ ^1P^o$  resonance (c.f. §2.4). The fundamental linear process has a kinetic energy release (KER) of about 5.4 eV, while the two-photon process has a KER of 35.4 eV. The measurable momenta for the processes are 0.63 au and 1.61 au. Ionization induced by the second harmonic also results in a momentum of 1.61 au. The distinction between both channels for individual events can be made by the two distinct momenta or energies of the ions. In this particular case it is very hard to differentiate between the two-photon process and the ionization via the second harmonic, as the KER is the same for both processes.

Instead of looking at individual events, we can look at the scaling of the

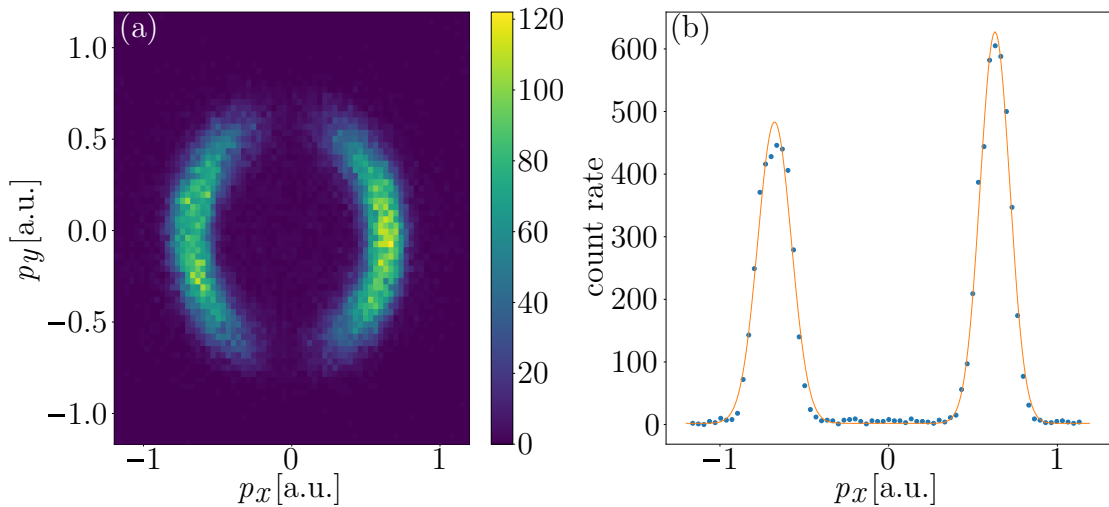


Figure 4.6: (a) The momentum distribution in the  $x - y$  plane in arbitrary units. The integration over the momentum in the  $z$  direction is done in a narrow band with  $|p_z| < 0.1$  au. (b) The momentum distribution in the  $x$  direction. The integration over both other axes is over  $|p_z|, |p_y| < 0.1$  au. The orange curve shows a fit with the sum of two Gaussians with a FWHM of 0.23 au for the negative direction and 0.20 au for the positive.

probability of an event with the pulse energy (c.f. §4.1.1). Compared to the trivial linear processes, the two-photon process scales quadratic. One finds no trivial scaling between the pulse energy in the fundamental wavelength and second harmonic[59, 60], the available data suggest a positive correlation[61]. The following analysis assumes that the partial pulse energy in the second harmonic wavelength scales linearly with the total pulse energy.

### 4.2.1 Linear process

The linear process discussed in this section is well understood. Exciting the ground state with a single photon, result in a angular momentum quantum number of  $l = 1$ . The total momentum is 0.63 au and the angular distribution is  $|Y_{1,0}(\theta)|^2 \propto \cos^2(\theta)$ . To observe the linear effect small pulse energies are sufficient.

The resulting 2d momentum in the  $x - y$  plane is shown in Figure 4.6 (a), where  $x$  is the axis of laser polarization. The angular distribution is well defined. We can recognize an asymmetry in the  $x$  direction. The reason for that is a known detector inefficiency at the point of impact for negative momenta.

For a more quantitative analysis, the one-dimensional momentum along the  $x$  direction is shown in Figure 4.6 (b). One can clearly see asymmetry between the positive and negative direction and the width of the momentum distribution. The width (FWHM) has been determined by a Gaussian fit and is 0.20 au for positive momenta. It depends on the temperature of the helium target, the bandwidth of the FEL, the intrinsic detector resolution and the flight distortion due to the Coulomb interaction between produced ions (see §4.2.2). For this measurement only small pulse energies are selected to suppress the last effect.

### 4.2.2 Space-charge effect

In general, particles with the same charge repel each other due to the Coulomb interaction. Therefore, a helium ion created in the focal spot of the laser perturbs the motion towards the detector for other ions produced in its vicinity. This effect, also called space-charge effect, limits the momentum resolution, especially for higher pulse energies where a lot of ions are created.

In Figure 4.7 the development of the space charge effect in the  $x - y$  plane for increasing pulse energies is depicted. Especially for high pulse energies, where we expect the highest contribution of two-photon ionization, the effect clearly distorts the momentum distribution.

In this work, the characterization of the space-charge effect is handled through inspecting the total momentum  $p_r = \sqrt{p_x^2 + p_y^2 + p_z^2}$ . Assuming that the effect is isotropic, there is no need for angular information. Similar to Figure 4.6(b), a gaussian fit is applied to measure the width of the momentum distribution and the mean momentum. The results for increasing pulse energies are shown in Figure 4.7. One can clearly see the linear increase in width and mean. While the discussion of the space-charge effect has been done only for the linear process, the results have a big impact for the two-photon process as well.

### 4.2.3 Two-photon process

In principle, the two-photon process is distinguishable from the linear process by the higher momentum of the ionized ion. The two-photon process has an intrinsic total momentum of 1.61 au. Because of the space-charge effect, the momentum

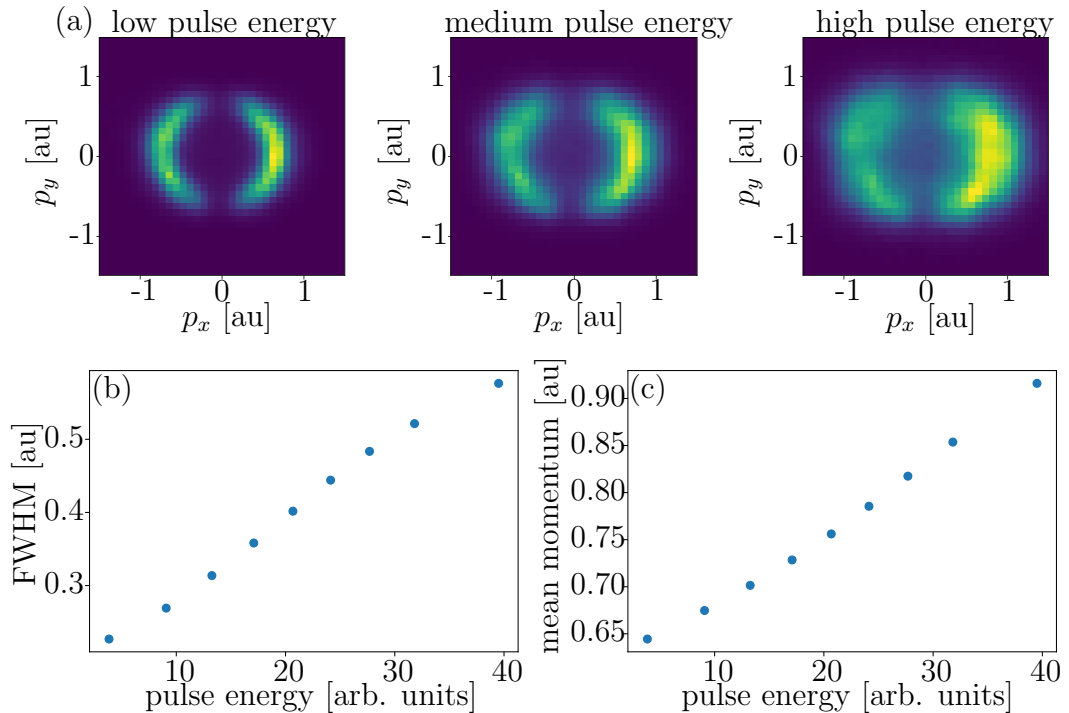


Figure 4.7: Upper panel (a) shows all events separated into three sets of equal size with low, medium and high pulse energies. The colormap is chosen linearly. The space charge clearly increases the width and distorts the momentum distribution. (b,c) This effect is characterized by the FWHM and mean of the distribution. Only events with positive momentum in the  $x$ -direction are considered, to suppress artifacts from the detector defect. The events are separated in nine same-sized sets with increasing pulse energy. (b) shows a linear increase of the width and therefore a loss in resolution. (c) The mean momentum of the distribution increases linearly with increasing pulse energy.

distribution of the linear effect spreads to higher momenta and overlaps with the signature of the two-photon momentum. At the same time, the space-charge effect increases the perceived momentum of the two-photon process. This means that for high pulse energies, where we expect the biggest contribution of nonlinear processes, the space-charge effect distorts the linear process such that a clear distinction between the two processes is more difficult. The following analysis, therefore, does not take into account individual events, but instead investigates at the scaling of the two-photon process with the pulse energy.

To account for the dominant linear process, a second order polynomial fit is applied to the logarithm of the momentum distribution. The logarithm of the

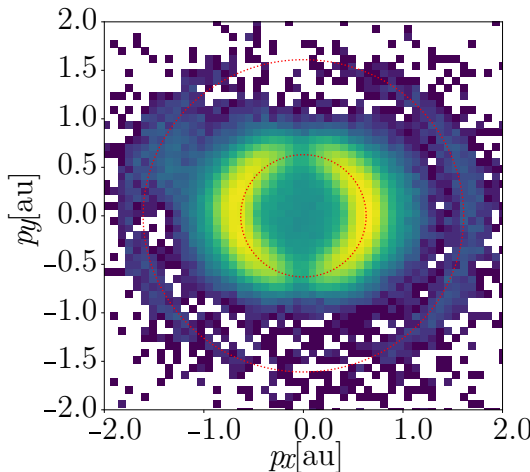


Figure 4.8: 2D  $x - y$  momentum distribution with logarithmic colormap. The inner red ring has a radius of 0.63 au and outer ring has a radius of 1.61 au for the two-photon or second harmonic process. The exemplary plot is for low pulse energy, where space charge effects do not play a big role. Instead, the second harmonic will has a big impact here.

momentum distribution is used, such that small deviations in the low density regions are weighed more in the fitting procedure. The region which is used for the fit is the falling edge of the single-photon peak(c.f. Figure 4.2.3(a)). The fit is then subtracted from the momentum distribution and the resulting distribution is integrated over the region of interest to receive the relative probability for the two-photon process.

A single-photon of the second harmonic will also ionize an electron with 1.61 au. This cannot be accounted for with a simple fitting procedure of the total momentum distribution. In §4.1.1, we showed that the one-photon process scales linearly with the pulse energy while the two-photon process scales quadratically. Assuming that the second harmonic's energy scales linearly with the total pulse energy, the second harmonic process scales linearly with the measured pulse energy. In summary, we expect the ratio  $R$  between  $N_2$ , the total probability of an event with a high momentum, and  $N_1$ , the probability of an fundamental one-photon event, to follow a linear function of the total pulse energy  $\mathcal{E}$ :

$$R(\mathcal{E}) = \frac{N_2}{N_1} = \frac{a\mathcal{E}^2 + b\mathcal{E}}{c\mathcal{E}} + d = A\mathcal{E} + B. \quad (4.7)$$

The physical parameter  $a$ ,  $b$  and  $c$  are dependent on the cross-section of the two-photon, second harmonic, one-photon processes and the pulse shape.  $A$  and  $B$  are linear fitting parameters. The slope  $A$  is the relative ratio between probabilities for the two-photon process and the fundamental one-photon process. The y-axis offset  $B$  gives us the relative second harmonic contribution and a possible flat background of residual gas.

#### 4. Above Threshold Ionization in Helium

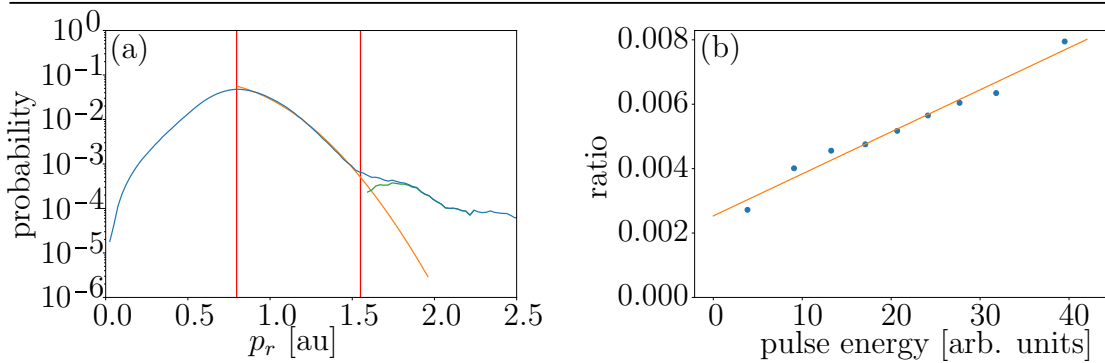


Figure 4.9: (a) Exemplary momentum distribution with logarithmic scale for high pulse energy. The red vertical lines depict the area used for the fit. The orange line depicts the fit and the green curve is the final two-photon/second harmonic contribution. (b) The ratio between events with a high momentum and events from the trivial linear process. Blue dots are the data points and the orange line is a linear fit  $f(x) = Ax + b$  with  $A = 1.31 \times 10^{-4}$  and  $B = 2.53 \times 10^{-3}$ .

Similar to Figure 4.7, the data set is divided into nine evenly sized sets with increasing pulse energy. For each data set, an individual fit is applied to account for the increasing space charge. The resulting ratio for each data set is plotted in Figure 4.9. The results shows a clear contribution of a nonlinear process.

### 4.3 Discussion and Outlook

A quantum few-level model simulation is used to show a technique to correlate individual recoil ion measurements with their corresponding FEL photon spectra to reconstruct the form of the two-photon resonance. The procedure relies on a clear distinction between nonlinear and linear processes. This has been complicated due to the space charge effect and large second-harmonic contribution. Nevertheless, the principle method could be demonstrated within the described constraints. The presented scheme is viable for other resonances as well and could be used for other measurements involving two-photon resonances excited by SASE FEL pulses.

Instead of looking at individual events, the total momentum distribution is taken into consideration. A fit was applied to account for the space-charge effect and to calculate the actual relative probability of non-trivial processes. The relative ratios between the non-trivial processes and trivial linear processes show

a linear scaling with the pulse energy. The non-zero slope is interpreted as a signature for nonlinear processes, while the significant y-axis offset is a clear signature for a linear contribution. A trivial increase due to the space-charge effect has been subtracted by carefully applying a least-squares fitting routine.

The linear contribution is assumed to come from the second-harmonic contribution. In this experiment, the actual strength of the second harmonic has not been measured. The linear scaling is a rough estimate and does not account for the complex origin [60]. Experimentally, the second harmonic could not be efficiently blocked using the available filter materials.

The pulse energy in the Reaction Microscope has not been directly measured. The used measure, given by the integrated spectra measured in the absorption beamline, is not calibrated to this point. The cross-section for linear processes is well known which can be used to reconstruct the pulse energy and to calibrate the pulse energy.

The available angular information of the momentum distribution given the REMI has not been taken into account. The angular distribution of the second-harmonic contribution is known and follows  $\cos^2 \theta$ . Using the different scaling relations with the pulse energy, a scheme to reconstruct the angular momentum distribution of the two-photon process could in principle be realized. A prediction for the angular distribution has been calculated by Wang and Greene[4]. The angular information would provide a valuable insight into the electronic configuration of the excited state before autoionizing.

Only a few experiments have been performed to observe the  $^1D^e 2p2p$  resonance. The only works we are aware of has been performed by Zitnik et al.[62] and Krässig et al [63]. No full three-dimensional momentum distribution has been measured, such that up to this point no measurement of the angular information has been performed at all.



# 5 Multi-Photon Double Ionization in Helium

While the first experiment is concerned with quasi-bound electron correlations in the form of autoionizing states, the second experiment deals with the interaction of electrons in their continuum states. **Two-photon double ionization (TPDI)** allows for highly correlated electrons even after ionization. Helium remains the benchmark system of choice given two free electrons and a doubly charged core.

For photon energies above 39.5 eV, the combined energy of two photons exceeds both the first ionization potential at 24.6 eV and the second at 54.4 eV. In this regime, for double ionization, both photons must be absorbed simultaneously in a direct process. For photon energies above the second ionization potential, the second photon can ionize the  $\text{He}^+$  ion individually. For these energies, the double ionization process can work sequentially. Close to the sequential edge, the sequential channel is visible through a virtual sequential process.

The here presented experiment takes advantage of the wavelength-tunability of FLASH 2 and is performed at four different photon energies. We start at 57 eV and measure the well understood sequential process. Furthermore the transition from the direct process 45.0 eV to the virtual sequential process at 53 eV is studied. Finally, the impact of resonance-enhanced three-photon sequential processes is investigated at a photon energy of 40.8 eV.

During the advent of high intensity XUV pulses TPDI has been the subject of intense theoretical studies [6, 9, 12, 20, 27–32, 64, 65]. Meanwhile, due to the complexity, only a few experiments were conducted [66–69]. Following on the trails of these pioneering studies, the presented experiment aims to increase the momentum resolution to set a new benchmark for current theory. A basic introduction into the current theoretical method is introduced in the initial section of this chapter, followed by the experiment results.

## 5.1 Ab initio theory

Simulating the two-photon double ionization provides a serious challenge. The following section will briefly introduce state-of-the-art theory using the time-dependent Schrödinger equation (TDSE) on a grid for each electron. With current computers, high accuracy can be reached. The following delineation will be along the lines of Refs. [6, 70] by Palacios et al, where more details can be found.

The TDSE is solved using the coupled atomic- and laser-interaction Hamiltonian in the dipole approximation (c.f. (2.5)). The electric field is hereby given by a sine-squared envelope, with a total duration  $T$

$$\mathbf{E}_\omega(t) = \hat{e}E_0 \sin^2\left(\frac{\pi}{T}t\right) \sin(\omega t). \quad (5.1)$$

Calculating the propagation of a wave packet, describing the motion of the electrons during the pulse is comparably easy. Usually, short few cycle pulses are used and only a few hundred timesteps are necessary to receive sufficient accuracy. However, after the pulse ends, the electrons are still interacting via the long-range Coulomb interaction. In principle, it would be necessary to calculate the propagation for times much larger than the pulse duration.

The method developed by Palacios et al. solves this problem by projecting the wave function  $\Psi(T)$  onto a scattering wave function  $\Psi_{sc}$ . The scattering wave function is given by outgoing-wave boundary conditions; however in practice this is very hard to realize. Implicitly this condition can also be applied by an exterior complex scaling (ECS):  $r \rightarrow R_0 + (r - R_0)e^{i\eta}$ , where  $R_0$  is the radius, beyond which the phase factor is applied.  $R_0$  should be chosen such that the propagation of the wave function during the pulse is contained in the interior region  $r < R_0$ .

The same problem can also be tackled by lowest-order perturbation theory to describe two-photon absorption[9, 32, 71]. This method involves the use of time-independent coupled Lewis-Dalgarno equations[72] and apply ECS for the correct boundary conditions.

In the definition of the generalized  $N$ -photon cross section, the rate of ejection is normalized to the  $N$ th power of the photon flux  $\Phi$ . In general, the cross-section depends on the pulse characteristic and only if perturbation theory is applicable, a generalized two-photon cross section can be constructed[6].

## 5.2 Experiment

In general, the TPDI-experiment works similar to the ATI experiment. In contrast to the ATI experiment, aluminum filters are used to attenuate the second and third harmonic of the FEL, as aluminum is highly absorbing for XUV-radiation with photon energy larger than  $\omega \geq 72 \text{ eV}$ . In addition, the doubly charged helium experiences a stronger force through the applied electric field in the REMI, as compared to the singly ionized helium. Therefore, the separation of the double ionization process from the singly ionized helium can be solved by applying a TOF condition.

Looking at the TOF-spectra (c.f. Figure 5.1), multiple peaks can be recognized. The TOF-spectrum is a histogram counting the ions that hit the detector after a time  $\Delta T$  after the triggering FEL pulse. The highest peak in the spectrum, appearing directly after the initial pulse, belongs to singly ionized helium. However, the ion already takes more time to reach the detector than the next FEL pulse. Therefore, one has to unwrap the TOF-spectra and assign the  $\text{He}^+$  ions to the respective previous pulse (c.f. Figure 5.1). The doubly ionized helium has a mass-to-charge ratio of  $m/Z = 2$  (mass in units of u) as compared to singly ionized helium with  $m/Z = 4$ . Therefore, the doubly charged helium is quicker by a factor of  $\sqrt{2}$  at the detector (c.f. (7.7)). This verifies that the peak at  $\sim 8900 \text{ ns}$  belongs to the doubly ionized helium. Most hits from residual gas particles are from hydrogen molecules. Linear interaction with the XUV pulses result in  $\text{H}_2^+$ . Having the same mass-charge ratio as doubly ionized helium, both arrive at the detector at the same time. The hydrogen can be observed as a broad distribution surrounding  $\text{He}^{++}$ . The TOF distribution is broader since the hydrogen molecules have neither the defined origin nor low temperature by the jet.

### 5.2.1 Sequential Ionization at 57 eV

The first presented measurement in this chapter is on sequential ionization at a photon energy of 57 eV. For the sequential process, the ionization of each electron can be considered to be independent from each other. The first ionized

## 5. Multi-Photon Double Ionization in Helium

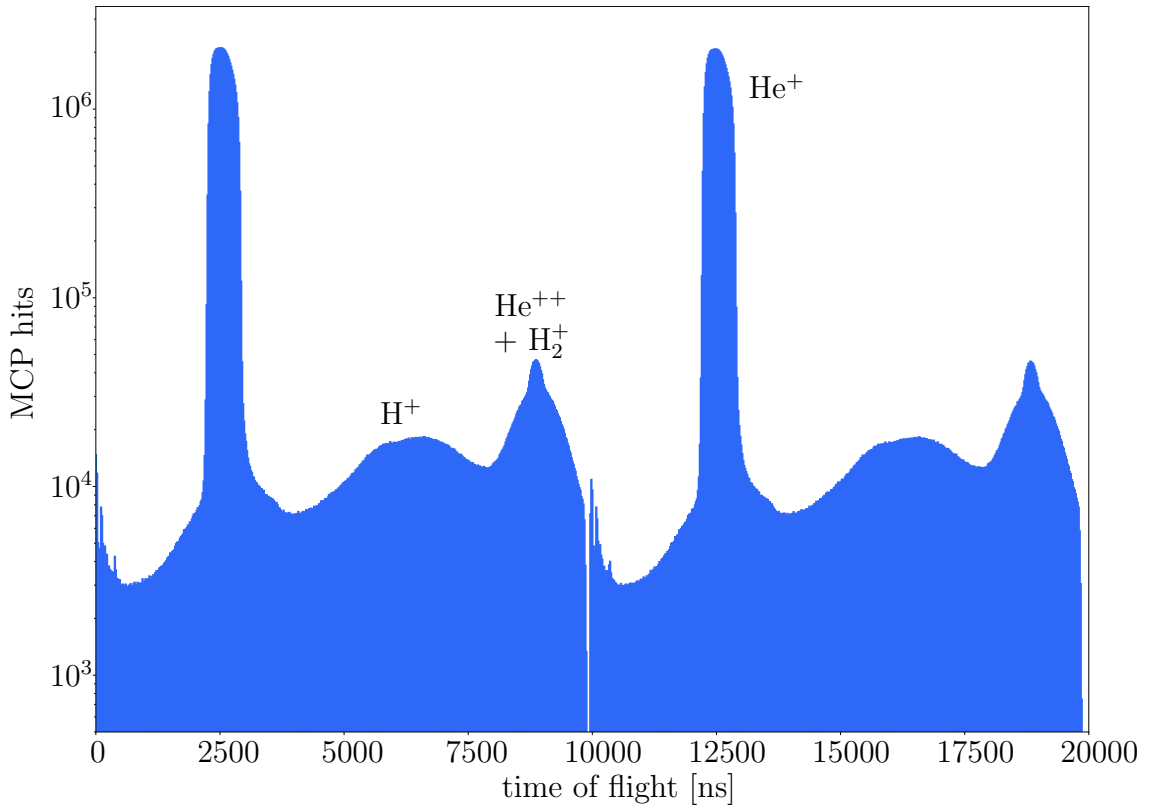


Figure 5.1: TOF mass spectrum for a photon energy of  $\omega = 53$  eV. First FEL-pulse at zero and second XUV-pulse at  $\sim 10\,000$  ns.  $\text{He}^+$  has a long TOF, such that it hits the detector only after the next XUV-pulse arrives.  $\text{He}^{++}$  recognizable on top of broad  $\text{H}_2^+$  background.

electron has a kinetic energy release of 32.4 eV. This can be translated into an initial ion momentum of 1.54 au. After absorption of a single photon the angular momentum quantum number is increased from  $l = 0$  to  $l = 1$ . Therefore, the angular dependence is given by the usual dipole pattern (which is similar to the single-photon process §4.2.1). After some time  $\Delta t$ , the electron is situated in the ground state of the helium ion which is the  $1s$  configuration with  $l = 0$ . Therefore, the second electron is also ionized with in a dipole pattern. The second electron has a kinetic energy release (KER) of 2.6 eV and a momentum of 0.44 au.

The final ion momentum is the result of adding up both electron momentum vectors. For both individual ionization processes the polarization direction of the laser is the favored direction of emission. Given a 50% chance to go either to the positive or negative  $x$ -direction for both processes, the combination yields four final peaks. For example, the first recoil-ion momentum peak furthest in the negative  $x$ -direction results from both the initial and second electron momenta

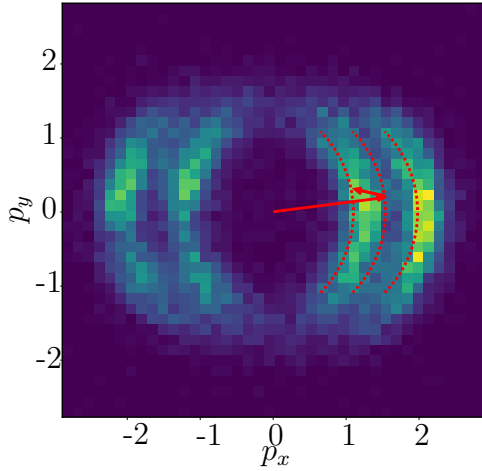


Figure 5.2: The momentum distribution of  $\text{He}^{++}$  at 57 eV in the  $x-y$  plane given in arbitrary units. The  $z$ -direction is cut close to zero. The three red semi circles have a radius of 1.54 au with either 0.44 au subtracted or added in the  $x$ -direction. The four peaks have a higher momentum than calculated due to the space-charge effect increasing the perceived momentum.

pointing in the positive direction. The next peak results from the second electron momentum instead pointing in the negative  $x$ -direction and so on.

The results are qualitatively compared with the theoretical results from Horner et al.[9], calculating the recoil-ion momenta for 58 eV with lowest order perturbation theory. Theory predicts the same four-peak structure. At the same time, the direct process is calculated to be negligible, which is in good agreement with the observed experimental results (compare with the direct process dominating in the next section §5.2.2). Correlation between the two electrons are only expected for pulse lengths on order of 1 fs and shorter[6]. Correlated electrons would preferably be ejected back-to-back due to the repulsive Coulomb interaction. This would be seen in the recoil-ion momenta in stronger inner rings compared to the outer rings. The experimental results do not show any significant difference in the peak strength.

### 5.2.2 Direct Double Ionization at 45 eV

If the photon energy is below the  $\text{He}^+$  ionization threshold, the ion can not be ionized further by an individual second photon. For two photons to simultaneously ionize both electrons, the electrons have to share the energy by interacting with each other. If both photons interact with the atom at the same time, correlation between the electrons is strongest, as both electrons are still bound closely to the core. In principle, the ratio of energies between electron one and two is

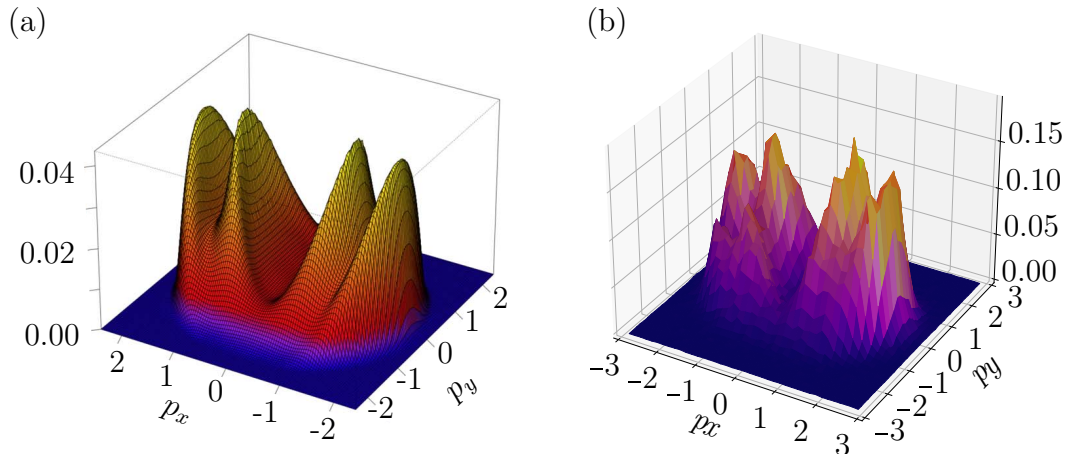


Figure 5.3: The momentum distribution of  $\text{He}^{++}$  in the sequential photon energy regime. (a) Recoil-ion cross-section calculated by Horner et al. with a photon energy of 58 eV adapted from Ref.[9]. (b) Comparable experimental results with 57 eV. The  $p_z$ -axis is projected onto the  $x - y$  plane. And the height axis of the plot shows the normalized event rate. Please note the different scales in the momentum axes.

arbitrary as long as both electrons have a positive final energy. Otherwise, one of them is captured again by the nucleus. For two photons with 45 eV each the total energy is 11 eV above the double ionization threshold of 79.0 eV. If only one of the ionized electrons receives the total remaining energy, one expects an recoil-ion momentum of 0.9 au. However, this would be extremely unlikely because the Coulomb interaction couples both two electrons with each other and forces them into opposite directions with equal momenta.

After absorption of two photons, the symmetry of the electron configuration is even. Starting from a  $^1S^e$  symmetry, the final configuration can be in a superposition of  $^1S^e$  and  $^1D^e$ . The individual electron momenta have not been measured, but only the final recoil-ion momentum. If the electrons are in the  $^1S^e$  configuration, the ejection would be completely isotropic. In this case, the recoil-ion momentum distribution would also be isotropic. In comparison, electrons in the  $^1D^e$  configuration have a preferred axis given by the polarization of the laser.

In Figure 5.4, the recoil-ion momentum, measured at a photon energy of 45 eV, is compared with the lowest order perturbation calculation by Horner et al. for 44 eV[9]. The experimental result shows only a minor asymmetry,

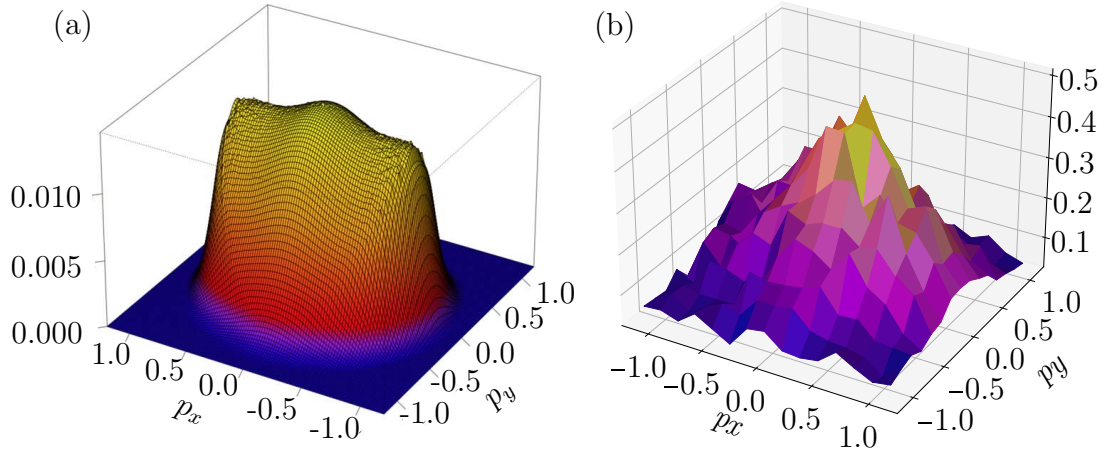


Figure 5.4: The momentum distribution of  $\text{He}^{++}$  in the direct photon energy regime. Figure (a) shows the differential cross-section calculated by Horner et al. with a photon energy of 44 eV adapted from Ref.[9]. This is compared to Figure (b), the experimentally found probability density for a central photon energy of 45 eV. The  $z$ -axis is projected onto the  $x - y$  plane. A qualitative comparison shows deviations between the two distributions.

while the theoretical predictions show unambiguous shoulders extending in the polarization direction. This is a clear signature of the virtual sequential ionization process which will be discussed in more detail in the following section §5.2.3. It seems like the calculations overestimates the contribution of this process.

### 5.2.3 Virtual sequential Ionization at 53 eV

At 53 eV the photon energy is close to the sequential ionization threshold of 54.4 eV. The bandwidth of the FEL of  $\sim 500$  meV ensures no trivial sequential process is possible. However, for photon energies close to the second ionization threshold, only a small energy transfer between the electrons is necessary to overcome the threshold.

When the first electron is ionized, the second electron is not immediately in the ground state of the  $\text{He}^+$  ion. Instead, directly after the ionization process, the state of the second electron has a rather broad energy distribution. Therefore, after absorption of another photon, the second electron can have enough energy to overcome the ionization threshold. In this sense, the interaction between electrons prior to ionization leads to the necessary energy sharing between the two.

## 5. Multi-Photon Double Ionization in Helium

---

Over time the energy distribution gets narrower until, in equilibrium, the second electron is in the ground state of the  $\text{He}^+$  ion with a defined energy.

This process, also called virtual sequential process, has a signature quite similar to that of the sequential ionization. The electrons are emitted independently from each other with a big difference in their free energy. The biggest contribution to the ion momentum is given by the first electron emitted in the usual dipole pattern in the direction of the laser polarization. In principle the second electron is also emitted in the same shape, but the proximity of the first electron still affects the ionization process such that back-to-back emission is still favored[6, 65].

The proximity of the first electron and its on the second ionization process depends strongly on the arrival time of the second photon. Likewise, the energy distribution of the second electron after ionization tends to lower energies the later another photon arrives. That means that in contrast to the trivial sequential double ionization the momentum distribution is highly dependent on the pulse structure, especially the pulse length[65].

The first comparison in Figure 5.5 is between the experimental data and the lowest order perturbation theory by Horner et al.[9]. In contrast to the experimental data, the calculations predict a four peak structure. The theoretical structure forms because the recoil-ion momentum of the second electron splits up the momentum distribution of the first electron similar to the trivial sequential process (see also §5.2.1). At the same time, the perturbation theory calculation shows a higher contribution of recoil-ions with a small momentum. This results from two electrons sharing their energy and moving into opposite directions. This contribution implies a high probability for two photons ionizing both electrons simultaneously similar to the direct process observed for a photon energy of 45 eV.

Figure 5.6 shows the recoil-ion momentum distribution for a photon energy of 52 eV calculated by solving the full TDSE by Horner et al [65]. The TDSE was solved using 1 fs and 2 fs pulses. The calculation shows significant differences for the two pulse lengths and suggests a higher contribution of the virtual sequential process for increased pulse duration. The experimental pulses were  $\sim 50$  fs and follow a stochastic complex time dependence. In principle, an even higher



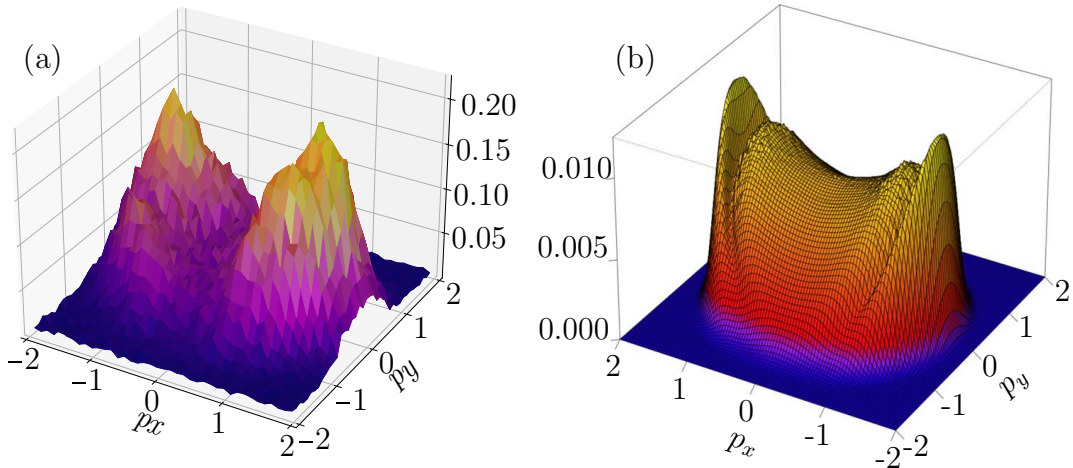


Figure 5.5: Comparison between experimental data (a) at 53 eV and perturbation theory (b) calculated by Horner et al[9] for 52 eV. The z-axis is projected onto the  $x - y$  plane.

contribution of the virtual sequential process is expected.

It should be noted that in the vicinity of the central photon energy multiple  $\text{He}^+$  ion resonances can enhance the three-photon sequential double ionization through the absorption of two-photons by the second electron. The signature of this process involves high momenta at  $3.39 \text{ au}^1$ , but no contributions have been found.

#### 5.2.4 Resonant three-photon sequential double ionization at 40.8 eV

Up to this point only double ionization using two photons has been discussed. Especially for the non-sequential regime between 39.5 eV and 54.6 eV, a process involving a third photon can become relevant. Ionizing the first electron individually and the second electron with another two photons we get a three-photon sequential double ionization. In principle, this process is very unlikely for the intensities discussed in this work, but the probability for the second ionization can be enhanced by a resonance of the  $\text{He}^+$  ion. The resonance serves as an intermediate state such that no direct two-photon process is necessary for the second ionization.

<sup>1</sup>The three-photon process is studied at 40.8 eV. Compare with the following section §5.2.4.

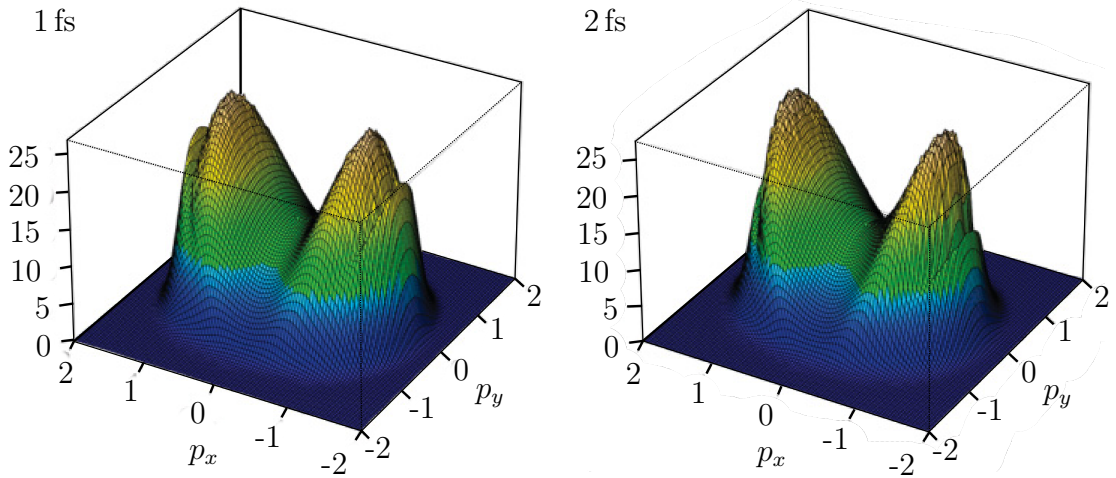


Figure 5.6: Simulation to calculate the recoil-ion momentum distribution using the TDSE for 1 fs and 2 fs pulses with a central photon energy of 52 eV by Horner et al[65].

This three-photon effect becomes relevant just above 39.5 eV, where the two-photon cross-section is small. The energetically lowest photon resonance in the  $\text{He}^+$  ion is the  $2p$  resonance at 40.8 eV. The  $2p$  state is quite long-lived and, therefore, is an ideal intermediate state before another photon can ionize the helium for a second time.

The first electron emission is a dipole emission with a KER of 16.2 eV and a momentum of 1.1 au. The second ionization has to be into an even state given that two photons are necessary with 27.2 eV and 1.4 au. The recoil-ion momentum is given by adding up both momenta similar to the two-photon sequential double ionization §5.2.1. Different from the two-photon sequential ionization §5.2.1, the second recoil momentum is higher. The direct two-photon process is still apparent in the momentum distribution with a contribution to small ion momenta in the center of the distribution.

Figure 5.7(a) shows the momentum distribution in the  $x - y$  plane. The red arrows mark the first electron recoil momentum in the laser polarization direction, while the red circle marks the corresponding possible recoil from the second electron emission. Especially the high momentum contribution at  $\pm 2.5$  au in the  $x$ -direction is a clear signature for the three-photon process, as it would be impossible to reach momenta that high with only two photons. In Figure 5.7(b)

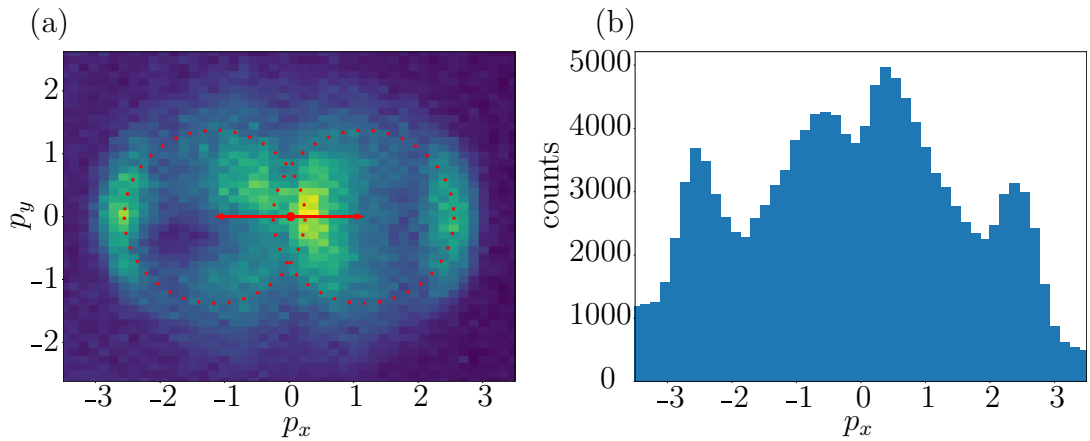


Figure 5.7: (a) The measured occurrence of momenta in the  $x - y$  plane of  $\text{He}^{++}$  with the  $z$ -axis integrated. The red arrows marks the initial ionization momentum of the first electron in the favored polarization direction. The dotted circles surrounding the arrowheads show the subsequent momentum of the second electron. (b) A slice through the two-dimensional momentum distribution along the polarization axis.

the momentum distribution is projected onto the  $x$ -axis. The two peaks in the center of the distribution are broader and stronger since they are amplified by the direct two-photon process. The distinction of both processes close to zero ion momenta is only possible by measuring the individual electron momenta.

The three-photon process can also be observed for smaller photon energies of 39.7 eV (c.f. Figure 5.8). The vicinity to the stable  $2p$  state leads to an increased lifetime of the virtual state and therefore an increased cross-section for the three-photon process. For 39.7 eV, the direct two-photon double ionization cross-section vanishes due to the limited phase space which is available for final states.

### 5.3 Discussion and Outlook

We have measured the recoil-ion momentum distribution of  $\text{He}^{++}$  for four different photon energies. For each photon energy different processes dominate which are further investigated. Theory predictions using lowest-order perturbation theory and solutions to the TDSE are compared with the experimental results. The theories are calculated for slightly different wavelengths, but the regime can be

considered noncritical such that no big deviations are expected. A quantitative comparison using calculations with the experimental available pulse duration and wavelength can be expected to show interesting deviations. However through a qualitative comparison interesting deviations and behavior can be observed.

The sequential process has been measured for 57 eV and Horner et al calculated the recoil-ion cross-section with lowest order perturbation theory for 58 eV. Compared to theory and classic estimation, the experiment shows higher momenta than expected. The reason for this is most probably that the space-charge spreads out the individual ions, which is perceived as a higher momentum (c.f. §4.2.2). Neither theory nor experiment suggest a noteworthy contribution of a direct process and time-dependent theory predict electron correlation effects only for pulse lengths below 1 fs[6].

At 45 eV, the direct process has been measured. Lowest order perturbation theory was applied at slightly lower photon energies of 44 eV, by Horner et al[9]. Horner et al. predict a contribution of the virtual sequential process, visible in the polarization direction of the momentum distribution, while the experimental results show only a minor contribution. In principle, the ratio between the direct and virtual sequential process depends on the pulse duration[6, 65]. For the long pulse duration in the experiment, one expects an even stronger contribution of the virtual sequential channel, when compared to the behavior at 52 eV.

In contrast to the measurement at 45 eV, we measured a high contribution of the virtual sequential process for a photon energy of 53 eV. Lowest order perturbation theory as well as a previous experiment[57] show a smaller virtual sequential contribution as compared to this experiment. Two different channels contribute in creating the final electron momentum distribution. For the direct process, two photons have to be absorbed together. In contrast to this, the two photons in the virtual sequential process have a finite time delay between them. Time-dependent theory shows a higher contribution of uncorrelated electrons for increasing pulse length [6]. Qualitatively our measurement supports the time-dependent solutions for 1 fs and 2 fs at 52 eV, while for a quantitative comparison a simulation using the pulse parameters of the experiment would be necessary to describe the actual experimental system.

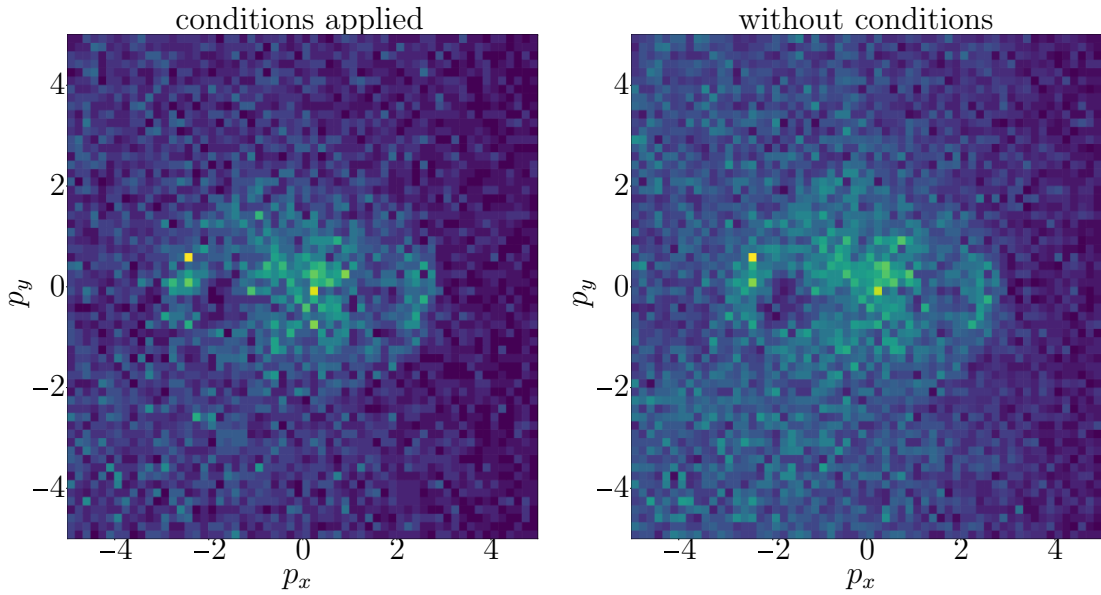


Figure 5.8: The measured occurrence of momenta in the  $x - y$  plane of  $\text{He}^{++}$  with the  $z$ -axis integrated at 39.7 eV. The cross-section for the two-photon process, as well as for the three photon process, is small compared to the linear background. A condition for a maximal variance of the Fourier spectrum is set to search for short pulses. In addition, the pulse energy is limited given a minimum value. The left plot shows the momentum distribution after both conditions are applied while the right plot shows the original data with only a TOF condition applied to select  $\text{He}^{++}$ .

The photon spectra carry a lot of information about the incoming pulses. For example, the Fourier transform of the photon spectra can be used to get information of the pulses in the time domain. Even though the phase information is lost, the distance in time between two sub pulses is reflected in a peak of the Fourier spectrum. Hereby, a small variance of the Fourier spectrum in the time domain corresponds to a short pulse duration, which in turn results in increased nonlinear effects. Using the variance as an external sorting parameter, therefore, increases the contrast of the momentum distribution by reducing the background. The procedure has been done for the measurement at a central photon energy of 39.7 eV (c.f. Figure 5.8), where the nonlinear event rate is small compared to the linear background. This results in an increased contrast and serves as a first proof of principle.

## 6 Conclusions

The first objective of this thesis has been the planning, setup and commissioning of a transient absorption spectroscopy beamline behind the REMI at FLASH2. The experimental setup has been designed to perform shot-to-shot photon spectroscopy in parallel with the REMI, as well as transient absorption spectroscopy individually. The commissioning measurements show a photon energy resolution of 33 meV at a central photon energy of 30 eV. Even for a high repetition rate of 100 kHz, the high frequency detector setup utilizing a GOTTHARD detector is capable of recording each individual FEL pulse.

The combined setup of REMI and transient absorption beamline has much more possibilities of use than described within this thesis. In principle, independent measurements using REMI and an absorption target in parallel are conceivable. However, the absorption target will become noticeable as background in the REMI due to the high pressure in the absorption cell. In addition, a high-harmonic source is available at the beamline to perform synchronized pump-probe experiments together with the FEL[73]. A recent experiment using this particular transient absorption beamline has been the first to realize a pump-probe scheme with FEL as pump and high-harmonic generation as probe, but is beyond the scope of this work. Meanwhile, the REMI has been used to get information on the existence and ratio of different ion species, which are probed in the absorption target.

The second part of this thesis has been the study of single and double ionization of helium. The high intensity FEL pulses allowed to observe nonlinear multi-photon channels. The first nonlinear ionization channel studied has been the resonant two-photon transition from the ground state into the  $^1D^e 2p2p$  state. Numerical analysis show a proof-of-concept to resolve a two-photon resonance well below the bandwidth of the FEL using self-convoluted spectra. The first experimental results show a clear signature of a nonlinear channel. To the best of our knowledge, neither the shape of the resonance nor the angular emission distribu-

## 6. Conclusions

---

tion was experimentally observed before. Further analysis is needed to overcome the experimental hurdles of the space-charge effect and the second harmonic to use the previously presented technique.

The other multi-photon channels under investigation are doubly ionizing helium. There are two channels available for two-photon double ionization, the sequential and the direct process. Because ionization takes place on an ultra-short time scale, the sequential process can be observed for photon energies below the second ionization process. The wavelength tunability of FLASH2 was used to observe the change of the two contributions to the TPDI at different photon energies. Because of the non-perturbative regime in which the experiment took place, no unique two-photon cross section can be found. The perturbation theory approach[9] shows clear deviations when compared to the experimental findings even in a qualitative comparison. A quantitative comparison between time-dependent non-perturbative theory and experiment is difficult to perform due to the complex SASE structure of the FEL pulses. Nonetheless, the statistics and resolution surpasses previous experiments and a quantitative comparison between state-of-the-art time-dependent theory and experimental data can provide new insights.

The three-photon double ionization was surveyed at 40.8 eV, where the  $1s \rightarrow 2p$  resonance is. Even off-resonant, at a central photon energy of 39.7 eV, a clear signature of the three-photon process could be detected. The signature of the three-photon process has explicitly not been observed for photon energies in resonance with the other Rydberg states (e.g. 52.9 eV) due to the comparatively high cross-section of the two-photon process. For 39.7 eV, the linear background of the residual hydrogen molecules create an event rate similar to the actual double ionization of helium. Careful sorting for high intensity pulses, using the shot-to-shot photon spectra, provides increased contrast. In principle, this procedure can be applied to other REMI measurements in order to alleviate artifacts introduced by the stochastic fluctuations of the FEL.

## 7 Appendix

### 7.1 Momentum reconstruction in a Reaction Microscope

We will only discuss reconstruction of momenta without a magnetic field. Therefore this is only applicable for ion-only measurements. We assume the detector assigned TOF  $t$  and the two dimensional position  $x$  and  $y$  on the detector. The ion has an mass  $m$  and electric charge  $q$ .

The position on the detector can be easily calculated, whereat the jet velocity  $v_{jet}$  along  $x$  has to be included

$$x = \frac{t}{m} (p_x - mv_{jet}) \quad \text{and} \quad y = \frac{t}{m} p_y. \quad (7.1)$$

This can be rewritten to

$$p_x = m \left( \frac{x}{m} - v_{jet} \right) \quad \text{and} \quad p_y = m \frac{y}{t}. \quad (7.2)$$

In TOF direction the electric field  $E$  accelerates the ion over the whole distance to the detector  $l_z$ . The acceleration is given by:

$$\ddot{z} = \frac{qE}{m} = \frac{qU}{ml_z} \quad (7.3)$$

Integrating the equation two times from 0 to  $t$  results in:

$$l_z = \dot{z}_0 t + \frac{1}{2} \ddot{z}_0 t^2 \quad (7.4)$$

The momentum  $p_z = m\dot{z}_0$  is then:

$$p_z = \frac{l_z m}{t} - \frac{qUt}{2l_z} \quad (7.5)$$

Additionally one can solve (7.4) to get the time of flight:

$$t_{\pm} = \frac{2l_z m}{\sqrt{p_z^2 + 2mqU} \pm p_z}. \quad (7.6)$$

Assuming that the initial momentum is small compared to the momentum introduced by the external field, we can approximate:

$$t_{\pm} \propto \sqrt{m/q} \quad (7.7)$$

We can use (7.7) to assign peaks in a TOF histogram to different species.



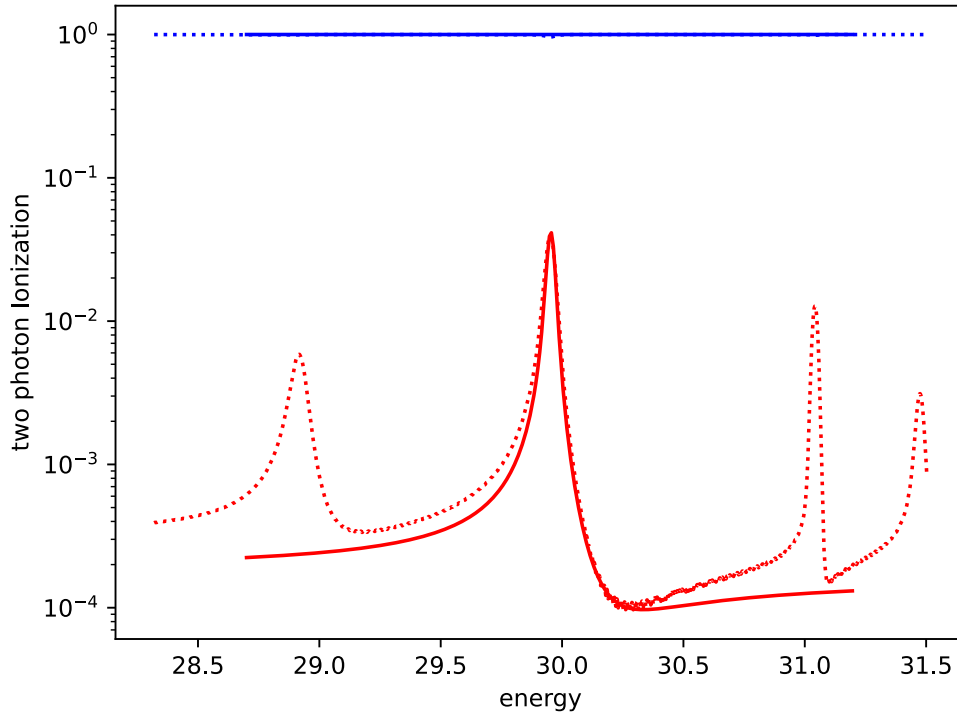


Figure 7.1: Simulated two photon ionization population. Dotted lines used the cross-section provided by Wang et al.[4] as described in §4.1.1. Full line used the same pulses in the four-level simulation.

## 7.2 Parameter of few-level system

The simulation has been done in Hartree atomic units[10].The few-level system describing the transition from the ground-state over a continuum to the  $^1D^e 2p^2$  state used the following values

Quantity	$E_0$	$E_c$	$E_e$	$\Gamma_1$	$\Gamma_2$	$V$	$d_{0-c}$	$d_{c-e}$	$d_{c-c^*}$
Numerical value in [au]	0.0	1.10	2.20	1.73	8.82	6.79e-2	1.20	1.00	0.119

The few-level system has been designed to fit a simulation using the rate equations (2.8) and (2.10) and the cross-section provided by Wang et al.[4] in a similar way described in §4.1.1. The four-level model shows similar behavior and reasonably simulate the system.

### 7.3 Split step method

The split step method is a numerical solution to the time dependent Schrödinger equation. It works quite similar to the Fourier-split-step method. We assume the Hamiltonian is separable between an time independent part  $\mathcal{H}_0$  and  $\mathcal{H}_I$ , which is linear in some time dependent scalar function  $f(t)$ :

$$\mathcal{H}(t) = \mathcal{H}_0 + f(t)h_I \quad (7.8)$$

We can generally solve the TDSE by

$$\Psi(t) = \int_{t_0}^t dt' \exp\left(-\frac{i}{\hbar}[\mathcal{H}_0 + f(t')h_I] t'\right) \Psi(t_0) \quad (7.9)$$

The solution can be discretized and the Baker-Hausdorff formula can be applied. This results in the numerical split-step method:

$$\Psi(t_n) \approx e^{-\frac{i}{\hbar}f(t_{n-1})h_I\Delta t} e^{-\frac{i}{\hbar}\mathcal{H}_0\Delta t} e^{-\frac{i}{\hbar}f(t_{n-2})h_I\Delta t} e^{-\frac{i}{\hbar}\mathcal{H}_0\Delta t} \dots e^{-\frac{i}{\hbar}f(t_0)h_I\Delta t} e^{-\frac{i}{\hbar}\mathcal{H}_0\Delta t} \Psi(t_0) \quad (7.10)$$

The error is of order  $\mathcal{O}(\Delta t^2)$  and can be improved to order  $\mathcal{O}(\Delta t^3)$  by simple symmetrization.

$$e^{-\frac{i}{\hbar}[\mathcal{H}_0+f(t')h_I]\Delta t} = e^{-\frac{i}{\hbar}\mathcal{H}_0\frac{\Delta t}{2}} e^{-\frac{i}{\hbar}f(t')h_I\Delta t} e^{-\frac{i}{\hbar}\mathcal{H}_0\frac{\Delta t}{2}} \quad (7.11)$$

For finite systems, the exponential function can easily be applied by matrix diagonalization. The transformation is simply given by a matrix of the eigenvectors  $M_0$ , while a transformation back would be the inverse.

The crucial trick is, that the transformation of the time dependent part  $f(t)h_I$  is only dependent on  $h_I$  and therefore static in time. The costly matrix diagonalization has to be done only once for all times.

The transformation from the diagonal space of  $H_0$  to the diagonal space of  $h_I$  is given by:

$$T_{I-0} = M_I M_0^{-1} \quad (7.12)$$

Each time step can be calculated with:

$$U(t_i) = T_{0-I} e^{-\frac{i}{\hbar}f(t_i)h_I\Delta t} T_{I-0} e^{-\frac{i}{\hbar}\mathcal{H}_0\Delta t} \quad (7.13)$$

assuming we start in the diagonal space of  $H_0$ .

# Bibliography

- [1] S. Schreiber and B. Faatz, “The free-electron laser FLASH,” *High Power Laser Science and Engineering*, vol. 3, 2015/ed.
- [2] R. Moshhammer, M. Unverzagt, W. Schmitt, J. Ullrich, and H. Schmidt-Böcking, “A  $4\pi$  recoil-ion electron momentum analyzer: A high-resolution “microscope” for the investigation of the dynamics of atomic, molecular and nuclear reactions,” *Nuclear Instruments and Methods in Physics Research Section B: Beam Interactions with Materials and Atoms*, vol. 108, pp. 425–445, Mar. 1996.
- [3] U. Fano, “Effects of Configuration Interaction on Intensities and Phase Shifts,” *Physical Review*, vol. 124, pp. 1866–1878, Dec. 1961.
- [4] Y. Wang and C. H. Greene, “Two-photon above-threshold ionization of helium,” *Physical Review A*, vol. 103, p. 033103, Mar. 2021.
- [5] E. Fomouo, P. Antoine, B. Piraux, L. Malegat, H. Bachau, and R. Shake-shaft, “Evidence for highly correlated electron dynamics in two-photon double ionization of helium,” *Journal of Physics B: Atomic, Molecular and Optical Physics*, vol. 41, p. 051001, Feb. 2008.
- [6] A. Palacios, D. A. Horner, T. N. Rescigno, and C. W. McCurdy, “Two-photon double ionization of the helium atom by ultrashort pulses,” *Journal of Physics B: Atomic, Molecular and Optical Physics*, vol. 43, p. 194003, Sept. 2010.
- [7] J. M. Feagin and J. S. Briggs, “Molecular-orbital description of the states of two-electron systems,” *Physical Review A*, vol. 37, pp. 4599–4613, June 1988.
- [8] C. D. Lin, “Hyperspherical coordinate approach to atomic and other Coulombic three-body systems,” *Physics Reports*, vol. 257, pp. 1–83, June 1995.

- [9] D. A. Horner, T. N. Rescigno, and C. W. McCurdy, “Decoding sequential versus nonsequential two-photon double ionization of helium using nuclear recoil,” *Physical Review A*, vol. 77, p. 030703, Mar. 2008.
- [10] D. R. Hartree, “The Wave Mechanics of an Atom with a Non-Coulomb Central Field. Part I. Theory and Methods,” *Mathematical Proceedings of the Cambridge Philosophical Society*, vol. 24, pp. 89–110, Jan. 1928.
- [11] D. I. R. Boll, O. A. Fojón, C. W. McCurdy, and A. Palacios, “Angularly resolved two-photon above-threshold ionization of helium,” *Physical Review A*, vol. 99, p. 023416, Feb. 2019.
- [12] A. S. Simonsen, S. Askeland, and M. Førre, “Two-photon double ionization of helium: Investigating the importance of correlation in the final state,” *Central European Journal of Physics*, vol. 11, pp. 1099–1106, Sept. 2013.
- [13] R. Shakeshaft, “Two-photon single and double ionization of helium,” *Physical Review A*, vol. 76, p. 063405, Dec. 2007.
- [14] E. Schrödinger, “Quantisierung als Eigenwertproblem,” *Annalen der Physik*, vol. 384, no. 4, pp. 361–376, 1926.
- [15] I. I. Rabi, “Space Quantization in a Gyration Magnetic Field,” *Physical Review*, vol. 51, pp. 652–654, Apr. 1937.
- [16] S. H. Autler and C. H. Townes, “Stark Effect in Rapidly Varying Fields,” *Physical Review*, vol. 100, pp. 703–722, Oct. 1955.
- [17] H.-P. Breuer and F. Petruccione, *The Theory of Open Quantum Systems*. Oxford University Press, 2007.
- [18] L. D. Landau and E. M. Lifshitz, *Quantum Mechanics Non-Relativistic Theory*. Butterworth-Heinemann, third edition ed., Jan. 1981.
- [19] L. W. Keldysh, “Ionization in the Field of a Strong Electromagnetic Wave,” *J. Exp. Theor. Phys.*, vol. 20, no. 5, pp. 1307–1314, 1965.

- [20] L. A. A. Nikolopoulos and P. Lambropoulos, “Multichannel theory of two-photon single and double ionization of helium,” *Journal of Physics B: Atomic, Molecular and Optical Physics*, vol. 34, pp. 545–564, Feb. 2001.
- [21] P. Agostini, F. Fabre, G. Mainfray, G. Petite, and N. K. Rahman, “Free-Free Transitions Following Six-Photon Ionization of Xenon Atoms,” *Physical Review Letters*, vol. 42, pp. 1127–1130, Apr. 1979.
- [22] H. Beutler, “Über Absorptionsserien von Argon, Krypton und Xenon zu Termen zwischen den beiden Ionisierungsgrenzen 2P<sub>3/2</sub>/0 und 2P<sub>1/2</sub>/0,” *Zeitschrift für Physik*, vol. 93, pp. 177–196, Mar. 1935.
- [23] K. Motomura, H. Fukuzawa, L. Foucar, X.-J. Liu, G. Prümper, K. Ueda, N. Saito, H. Iwayama, K. Nagaya, H. Murakami, M. Yao, A. Belkacem, M. Nagasono, A. Higashiya, M. Yabashi, T. Ishikawa, H. Ohashi, and H. Kimura, “Multiple ionization of atomic argon irradiated by EUV free-electron laser pulses at 62 nm: Evidence of sequential electron strip,” *Journal of Physics B: Atomic, Molecular and Optical Physics*, vol. 42, p. 221003, Nov. 2009.
- [24] K. Motomura, H. Fukuzawa, S.-K. Son, S. Mondal, T. Tachibana, Y. Ito, M. Kimura, K. Nagaya, T. Sakai, K. Matsunami, S. Wada, H. Hayashita, J. Kajikawa, X.-J. Liu, R. Feifel, P. Johnsson, M. Siano, E. Kukk, B. Rudek, B. Erk, L. Foucar, E. Robert, C. Miron, K. Tono, Y. Inubushi, T. Hatsui, M. Yabashi, M. Yao, R. Santra, and K. Ueda, “Sequential multiphoton multiple ionization of atomic argon and xenon irradiated by x-ray free-electron laser pulses from SACLA,” *Journal of Physics B: Atomic, Molecular and Optical Physics*, vol. 46, p. 164024, Aug. 2013.
- [25] M. A. Kornberg and P. Lambropoulos, “Photoelectron energy spectrum in \textasciigravedirect\textquotesingle two-photon double ionization of helium,” *Journal of Physics B: Atomic, Molecular and Optical Physics*, vol. 32, pp. L603–L613, Oct. 1999.
- [26] K. Schulz, G. Kaindl, M. Domke, J. D. Bozek, P. A. Heimann, A. S. Schlachter, and J. M. Rost, “Observation of New Rydberg Series and Reso-

- nances in Doubly Excited Helium at Ultrahigh Resolution,” *Physical Review Letters*, vol. 77, pp. 3086–3089, Oct. 1996.
- [27] A. S. Kheifets and I. A. Ivanov, “Convergent close-coupling calculations of two-photon double ionization of helium,” *Journal of Physics B: Atomic, Molecular and Optical Physics*, vol. 39, pp. 1731–1742, Mar. 2006.
- [28] L. A. A. Nikolopoulos and P. Lambropoulos, “Time-dependent theory of double ionization of helium under XUV radiation,” *Journal of Physics B: Atomic, Molecular and Optical Physics*, vol. 40, pp. 1347–1357, Mar. 2007.
- [29] S. X. Hu, J. Colgan, and L. A. Collins, “Triple-differential cross-sections for two-photon double ionization of He near threshold,” *Journal of Physics B: Atomic, Molecular and Optical Physics*, vol. 38, pp. L35–L45, Dec. 2004.
- [30] L. Feng and H. W. van der Hart, “Two-photon double ionization of He,” *Journal of Physics B: Atomic, Molecular and Optical Physics*, vol. 36, pp. L1–L7, Dec. 2002.
- [31] M. S. Pindzola and F. Robicheaux, “Two-photon double ionization of He and H<sup>+</sup>,” *Journal of Physics B: Atomic, Molecular and Optical Physics*, vol. 31, pp. L823–L831, Oct. 1998.
- [32] D. A. Horner, F. Morales, T. N. Rescigno, F. Martín, and C. W. McCurdy, “Two-photon double ionization of helium above and below the threshold for sequential ionization,” *Physical Review A*, vol. 76, p. 030701, Sept. 2007.
- [33] S. Schreiber, “The injector of the VUV-FEL at DESY,” *eConf*, vol. C0508213, no. FEL-2005-THPP038, p. THPP038, 2005.
- [34] K.-J. Kim, Z. Huang, and R. Lindberg, *Synchrotron Radiation and Free-Electron Lasers: Principles of Coherent X-Ray Generation*. Cambridge: Cambridge University Press, 2017.
- [35] B. W. J. McNeil and N. R. Thompson, “X-ray free-electron lasers,” *Nature Photonics*, vol. 4, pp. 814–821, Dec. 2010.

- [36] S. Düsterer, P. Radcliffe, G. Geloni, U. Jastrow, M. Kuhlmann, E. Plönjes, K. Tiedtke, R. Treusch, J. Feldhaus, P. Nicolosi, L. Poletto, P. Yeates, H. Luna, J. T. Costello, P. Orr, D. Cubaynes, and M. Meyer, “Spectroscopic characterization of vacuum ultraviolet free electron laser pulses,” *Optics Letters*, vol. 31, pp. 1750–1752, June 2006.
- [37] T. Pfeifer, Y. Jiang, S. Düsterer, R. Moshhammer, and J. Ullrich, “Partial-coherence method to model experimental free-electron laser pulse statistics,” *Optics Letters*, vol. 35, pp. 3441–3443, Oct. 2010.
- [38] R. Ivanov, J. Liu, G. Brenner, M. Brachmanski, and S. Düsterer, “FLASH free-electron laser single-shot temporal diagnostic: Terahertz-field-driven streaking,” *Journal of Synchrotron Radiation*, vol. 25, pp. 26–31, Jan. 2018.
- [39] G. Schmid, K. Schnorr, S. Augustin, S. Meister, H. Lindenblatt, F. Trost, Y. Liu, M. Braune, R. Treusch, C. D. Schröter, T. Pfeifer, and R. Moshhammer, “Reaction microscope endstation at FLASH2,” *Journal of Synchrotron Radiation*, vol. 26, pp. 854–867, May 2019.
- [40] G. Schmid, *Two-Color Pump-Probe Experiments on Small Quantum Systems at the Free-Electron Laser in Hamburg*. PhD thesis, Ruperto-Carola-University of Heidelberg, Heidelberg, June 2018.
- [41] G. Scoles, *Atomic and Molecular Beam Methods*. Oxford University Press, 1988.
- [42] L. Fechner, *High Resolution Experiments on Strong-Field Ionization of Atoms and Molecules: Test of Tunneling Theory, the Role of Doubly Excited States, and Channel-Selective Electron Spectra*. PhD thesis, Ruperto-Carola-University of Heidelberg, Heidelberg, Nov. 2014.
- [43] J. Ladislav Wiza, “Microchannel plate detectors,” *Nuclear Instruments and Methods*, vol. 162, pp. 587–601, June 1979.
- [44] M. Lampton, O. Siegmund, and R. Raffanti, “Delay line anodes for microchannel-plate spectrometers,” *Review of Scientific Instruments*, vol. 58, Jan. 1987.

- [45] T. Ding, C. Ott, A. Kaldun, A. Blättermann, K. Meyer, V. Stooss, M. Rebholz, P. Birk, M. Hartmann, A. Brown, H. V. D. Hart, and T. Pfeifer, “Time-resolved four-wave-mixing spectroscopy for inner-valence transitions,” *Optics Letters*, vol. 41, pp. 709–712, Feb. 2016.
- [46] T. Ding, M. Rebholz, L. Aufleger, M. Hartmann, K. Meyer, V. Stooß, A. Magunia, D. Wachs, P. Birk, Y. Mi, G. D. Borisova, C. d. C. Castanheira, P. Rupprecht, Z.-H. Loh, A. R. Attar, T. Gaumnitz, S. Roling, M. Butz, H. Zacharias, S. Düsterer, R. Treusch, S. M. Cavaletto, C. Ott, and T. Pfeifer, “Nonlinear Coherence Effects in Transient-Absorption Ion Spectroscopy with Stochastic Extreme-Ultraviolet Free-Electron Laser Pulses,” *Physical Review Letters*, vol. 123, p. 103001, Sept. 2019.
- [47] T. Ding, M. Rebholz, L. Aufleger, M. Hartmann, V. Stooß, A. Magunia, P. Birk, G. D. Borisova, D. Wachs, C. da Costa Castanheira, P. Rupprecht, Y. Mi, A. R. Attar, T. Gaumnitz, Z.-H. Loh, S. Roling, M. Butz, H. Zacharias, S. Düsterer, R. Treusch, A. Eislage, S. M. Cavaletto, C. Ott, and T. Pfeifer, “Measuring the frequency chirp of extreme-ultraviolet free-electron laser pulses by transient absorption spectroscopy,” *Nature Communications*, vol. 12, p. 643, Jan. 2021.
- [48] T. Ding, M. Rebholz, L. Aufleger, M. Hartmann, V. Stooß, A. Magunia, P. Birk, G. D. Borisova, C. d. C. Castanheira, P. Rupprecht, Y. Mi, T. Gaumnitz, Z.-H. Loh, S. Roling, M. Butz, H. Zacharias, S. Düsterer, R. Treusch, C. Ott, and T. Pfeifer, “XUV pump–XUV probe transient absorption spectroscopy at FELs,” *Faraday Discussions*, vol. 228, pp. 519–536, May 2021.
- [49] C. Ott, L. Aufleger, T. Ding, M. Rebholz, A. Magunia, M. Hartmann, V. Stooß, D. Wachs, P. Birk, G. D. Borisova, K. Meyer, P. Rupprecht, C. da Costa Castanheira, R. Moshhammer, A. R. Attar, T. Gaumnitz, Z.-H. Loh, S. Düsterer, R. Treusch, J. Ullrich, Y. Jiang, M. Meyer, P. Lambropoulos, and T. Pfeifer, “Strong-Field Extreme-Ultraviolet Dressing of Atomic Double Excitation,” *Physical Review Letters*, vol. 123, p. 163201, Oct. 2019.
- [50] L. Aufleger, “Measurement of electron dynamics in atoms and molecules with



- intense XUV FEL radiation,” *Master Thesis, Ruperto-Carola-University of Heidelberg*, 2016.
- [51] T. Kita, T. Harada, N. Nakano, and H. Kuroda, “Mechanically ruled aberration-corrected concave gratings for a flat-field grazing-incidence spectrograph,” *Applied Optics*, vol. 22, pp. 512–513, Feb. 1983.
- [52] M. Moszyński, T. Ludziejewski, D. Wolski, W. Klamra, and L. O. Norlin, “Properties of the YAG:ce scintillator,” *Nuclear Instruments and Methods in Physics Research Section A: Accelerators, Spectrometers, Detectors and Associated Equipment*, vol. 345, pp. 461–467, July 1994.
- [53] A. Mozzanica, A. Bergamaschi, R. Dinapoli, H. Graafsma, D. Greiffenberg, B. Henrich, I. Johnson, M. Lohmann, R. Valeria, B. Schmitt, and S. Xintian, “The GOTTHARD charge integrating readout detector: Design and characterization,” *Journal of Instrumentation*, vol. 7, pp. C01019–C01019, Jan. 2012.
- [54] S. Palutke, N. C. Gerken, K. Mertens, S. Klumpp, A. Mozzanica, B. Schmitt, C. Wunderer, H. Graafsma, K.-H. Meiwes-Broer, W. Wurth, and M. Martins, “Spectrometer for shot-to-shot photon energy characterization in the multi-bunch mode of the free electron laser at Hamburg,” *Review of Scientific Instruments*, vol. 86, p. 113107, Nov. 2015.
- [55] S. L. Sorensen, T. Åberg, J. Tulkki, E. Rachlew-Källne, G. Sundström, and M. Kirm, “Argon 3s autoionization resonances,” *Physical Review A*, vol. 50, pp. 1218–1230, Aug. 1994.
- [56] A. A. Sorokin, Y. Bican, S. Bonfigt, M. Brachmanski, M. Braune, U. F. Jastrow, A. Gottwald, H. Kaser, M. Richter, and K. Tiedtke, “An X-ray gas monitor for free-electron lasers,” *Journal of Synchrotron Radiation*, vol. 26, pp. 1092–1100, July 2019.
- [57] M. Kurka, *Zwei-Photonen-Doppelionisation von Helium Und D2-Molekülen Am Freie-Elektronen-Laser in Hamburg*. PhD thesis, Ruperto-Carola-University of Heidelberg, Heidelberg, July 2011.

- [58] I. J. B. Macias, S. Düsterer, R. Ivanov, J. Liu, G. Brenner, J. Rönsch-Schulenburg, M. K. Czwalińska, and M. V. Yurkov, “Study of temporal, spectral, arrival time and energy fluctuations of SASE FEL pulses,” *Optics Express*, vol. 29, pp. 10491–10508, Mar. 2021.
- [59] S. G. Biedron, R. J. Dejus, Z. Huang, S. V. Milton, V. Sajaev, W. Berg, M. Borland, P. K. Den Hartog, M. Erdmann, W. M. Fawley, H. P. Freund, E. Gluskin, K. – Kim, J. W. Lewellen, Y. Li, A. H. Lumpkin, E. R. Moog, A. Nassiri, G. Wiemerslage, and B. X. Yang, “Measurements of nonlinear harmonic generation at the Advanced Photon Source’s SASE FEL,” *Nuclear Instruments and Methods in Physics Research Section A: Accelerators, Spectrometers, Detectors and Associated Equipment*, vol. 483, pp. 94–100, May 2002.
- [60] G. Geloni, E. Saldin, E. Schneidmiller, and M. Yurkov, “Exact solution for second harmonic generation in XFELs,” *Optics Communications*, vol. 271, pp. 207–218, Mar. 2007.
- [61] S. Düsterer, “Personal communication,” 2021.
- [62] M. Žitnik, A. Mihelič, K. Bučar, M. Kavčič, J.-E. Rubensson, M. Svanquist, J. Söderström, R. Feifel, C. Sâthe, Y. Ovcharenko, V. Lyamayev, T. Mazza, M. Meyer, M. Simon, L. Journal, J. Lüning, O. Plekan, M. Coreno, M. Devetta, M. Di Fraia, P. Finetti, R. Richter, C. Grazioli, K. C. Prince, and C. Callegari, “High Resolution Multiphoton Spectroscopy by a Tunable Free-Electron-Laser Light,” *Physical Review Letters*, vol. 113, p. 193201, Nov. 2014.
- [63] B. Krässig, E. P. Kanter, S. H. Southworth, R. Guillemin, O. Hemmers, D. W. Lindle, R. Wehlitz, and N. L. S. Martin, “Photoexcitation of a Dipole-Forbidden Resonance in Helium,” *Physical Review Letters*, vol. 88, p. 203002, May 2002.
- [64] R. Shakeshaft, “Two-photon single and double ionization of helium,” *Physical Review A*, vol. 76, p. 063405, Dec. 2007.

- [65] D. A. Horner, T. N. Rescigno, and C. W. McCurdy, “Nuclear recoil cross sections from time-dependent studies of two-photon double ionization of helium,” *Physical Review A*, vol. 81, p. 023410, Feb. 2010.
- [66] A. Rudenko, L. Foucar, M. Kurka, T. Ergler, K. U. Kühnel, Y. H. Jiang, A. Voitkiv, B. Najjari, A. Kheifets, S. Lüdemann, T. Havermeier, M. Smolarski, S. Schössler, K. Cole, M. Schöffler, R. Dörner, S. Düsterer, W. Li, B. Keitel, R. Treusch, M. Gensch, C. D. Schröter, R. Moshhammer, and J. Ullrich, “Recoil-Ion Momentum Distributions for Two-Photon Double Ionization of He and Ne by 44 eV Free-Electron Laser Radiation,” *Physical Review Letters*, vol. 101, p. 073003, Aug. 2008.
- [67] M. Kurka, J. Feist, D. A. Horner, A. Rudenko, Y. H. Jiang, K. U. Kühnel, L. Foucar, T. N. Rescigno, C. W. McCurdy, R. Pazourek, S. Nagele, M. Schulz, O. Herrwerth, M. Lezius, M. F. Kling, M. Schöffler, A. Belkacem, S. Düsterer, R. Treusch, B. I. Schneider, L. A. Collins, J. Burgdörfer, C. D. Schröter, R. Moshhammer, and J. Ullrich, “Differential cross sections for non-sequential double ionization of He by 52\hspace0.167emeV photons from the Free Electron Laser in Hamburg, FLASH,” *New Journal of Physics*, vol. 12, p. 073035, July 2010.
- [68] P. Antoine, E. Fomouo, B. Piraux, T. Shimizu, H. Hasegawa, Y. Nabekawa, and K. Midorikawa, “Two-photon double ionization of helium: An experimental lower bound of the total cross section,” *Physical Review A*, vol. 78, p. 023415, Aug. 2008.
- [69] H. Shimada, K. Komatsu, W. Komatsubara, T. Mizuno, S. Miyake, S. Minemoto, H. Sakai, T. Majima, S. Owada, T. Togashi, M. Yabashi, and A. Yagishita, “Two- and three-photon double ionization of helium by soft x-ray free-electron laser pulses,” *Journal of Physics B: Atomic, Molecular and Optical Physics*, vol. 52, p. 065602, Mar. 2019.
- [70] A. Palacios, C. W. McCurdy, and T. N. Rescigno, “Extracting amplitudes for single and double ionization from a time-dependent wave packet,” *Physical Review A*, vol. 76, p. 043420, Oct. 2007.

- [71] D. A. Horner, F. Morales, T. N. Rescigno, F. Martín, and C. W. McCurdy, “Two-photon double ionization of helium above and below the threshold for sequential ionization,” *Physical Review A*, vol. 76, p. 030701, Sept. 2007.
- [72] A. Dalgarno, J. T. Lewis, and D. R. Bates, “The exact calculation of long-range forces between atoms by perturbation theory,” *Proceedings of the Royal Society of London. Series A. Mathematical and Physical Sciences*, vol. 233, pp. 70–74, Dec. 1955.
- [73] E. Appi, C. C. Papadopoulou, J. L. Mapa, N. Wesavkar, C. Jusko, P. Mosel, S. Ališauskas, T. Lang, C. M. Heyl, B. Manschwetus, M. Brachmanski, M. Braune, H. Lindenblatt, F. Trost, S. Meister, P. Schoch, R. Treusch, R. Moshhammer, I. Hartl, U. Morgner, and M. Kovacev, “A synchronized VUV light source based on high-order harmonic generation at FLASH,” *Scientific Reports*, vol. 10, p. 6867, Apr. 2020.

# Danksagung

An dieser Stelle möchte ich all jenen Danken, die mich während meines Studiums unterstützt haben und insbesondere während der Masterarbeit eine unerlässliche Hilfe waren:


- **Thomas Pfeifer** in dessen Abteilung ich meine Masterarbeit durchführen durfte. Vielen Dank für die vielen Tipps und Anregungen und dafür das du in deinem vollen Terminkalender immer Platz für mich gefunden hast.
- **Christian Ott** hatte mir die Möglichkeit gegeben und das Vertrauen geschenkt bei diesem großartigen Projekt in seiner Arbeitsgruppe mitzuarbeiten. Insbesondere möchte ich mich bei dir auch für die unzähligen und hilfreichen Diskussionen mit bedanken.
- **Robert Moshammer**, der das FLASH-REMI ins Leben gerufen hatte. Deine pragmatischen Ansätze und Herangehensweise haben uns oftmals viele Probleme gelöst.
- **Marc Rebholz** für die tolle Zusammenarbeit beim Aufbau des Experiments. Außerdem noch vielen Dank für die klasse Mitarbeit bei den Strahlzeiten und die Korrektur dieser Arbeit.
- **Thomas Ding** für all die Planung und Arbeit die du im Vorhinein in dieses Experiment gesteckt hast. Danke auch für die anfängliche Betreuung ohne die ich mich definitiv in diesem komplexen Feld nicht zurecht gefunden hätte.
- **Alex von der Dellen und Christian Kaiser** für eure technische Unterstützung ohne die der Aufbau des Experiments schlicht nicht möglich gewesen wäre.
- **Gergana D. Borisova** als Nebensitzerin im Büro, die ich immer wieder mit meinen kurzen (oder auch längeren) Fragen stören durfte. Ohne dich wäre die Auswertung, insbesondere in Go4 nicht so schnell vorangekommen.

- **Severin, Florian und Hannes** vom FLASH-REMI team. Ohne euch wäre niemand fähig gewesen das REMI zu betreiben.
- **Alex, Max, Patrick, Lennart, Paul, Sophia, Shuyuan und Paul** die während meiner Zeit am MPIK tolle Kollegen waren und mir immer mit gutem Rat zur Seite standen.
- **Meine Eltern**, die mich stets in allen meinen Entscheidungen unterstützt haben und auf die ich mich immer verlassen konnte.
- **Meine WG**, bei dir ich mein ganzes Studium gelebt habe. Danke für sechs tolle Jahre. Ich hätte nicht mehr Glück haben können als diese WG direkt zu Beginn meines Studiums zu finden.
- **Allen meinen Freunden**

## Erklärung

Ich versichere, dass ich diese Arbeit selbstständig verfasst und keine anderen als die angegebenen Quellen und Hilfsmittel benutzt habe.

Heidelberg, den 12.11.2021,

  
.....